LRRK2 G2019S kinase activity triggers neurotoxic NSF aggregation

Francesca Pischedda[1]*, Maria Daniela Cirnaru[2]*, Luisa Ponzoni[3], Michele Sandre[4], Alice Biosa[5], Maria Perez Carrion[1,6], Oriano Marin[4], Michele Morari[7], Lifeng Pan[8], Elisa Greggio[5], Rina Bandopadhyay[9], Mariaelvina Sala[3] and Giovanni Piccoli[1]#

1 CIBIO, Università degli Studi di Trento, Trento, Italy & Dulbecco Telethon Institute
2 Icahn School of Medicine at Mount Sinai, New York, USA
3 CNR, Institute of Neuroscience, Milan, Italy
4 Department of Biomedical Sciences (DSB), University of Padova, Italy
5 Department of Biology, University of Padova, Italy
6 Facultad de Farmacia, Universidad CEU San Pablo, Madrid, Spain
7 Department of Biomedical and Specialty Surgical Sciences, University of Ferrara, Italy
8 Shanghai Institute of Organic Chemistry, Shangai, China
9 Reta Lila Weston Institute of Neurological Studies and Department of Clinical and Movement Neuroscience, UCL Queen Square Institute of Neurology, London, UK

*equal contribution
corresponding author

Summary (max 150 words)
Parkinson's disease (PD) is characterized by the progressive degeneration of dopaminergic neurons within the substantia nigra pars compacta and the presence of protein aggregates in surviving neurons. LRRK2 G2019S mutation is one the major determinant of familial PD cases and leads to late-onset PD with pleomorphic pathology, including alpha-synuclein accumulation and deposition of protein inclusions. LRRK2 binds and phosphorylates N-ethylmaleimide sensitive factor (NSF). We observed aggregates containing NSF in basal ganglia specimens from G2019S carrier PD patients and in cellular and animal models expressing the LRRK2 G2019S variant. We found that LRRK2 G2019S kinase activity induces the accumulation of NSF in toxic aggregates. Noteworthy, the induction of autophagy cleared NSF aggregation and rescued motor and cognitive impairment observed in aged hG2019S BAC mice. We suggest that LRRK2 G2019S pathological phosphorylation hampers substrate catabolism, thus causing the formation of cytotoxic protein inclusions.

Highlights

- LRRK2 phosphorylates NSF in vivo
- NSF aggregates in complementary LRRK2 G2019S models
- LRRK2 G2019S kinase activity induces NSF accumulation in toxic aggregates
- Autophagy induction rescues hG2019S BAC mice motor and cognitive impairment

Introduction

Parkinson's disease (PD) is a heterogeneous movement disorder characterized by the progressive degeneration of dopaminergic neurons within the Substantia Nigra pars compacta (SNpc) and the formation of Lewy bodies containing alpha-synuclein in surviving dopaminergic neurons [reviewed in (Obeso et al. 2017)]. Mutations in LRRK2 gene (PARK8; OMIM 609007) are linked to late-onset autosomal dominant PD, accounting for up to 13% of familial PD cases compatible with dominant inheritance (Paisan-Ruiz et al. 2008) and 1 to 2% of sporadic PD patients (J. P. Taylor, Mata, e Farrer 2006). Clinically and pathologically, the features of LRRK2-associated parkinsonism are often indistinguishable from idiopathic PD [reviewed in (Whaley et al. 2006)]. Phylogenetically the LRRK2 kinase domain belongs to the TKL (tyrosine like kinases) and shows high similarity to Mixed lineage kinases (MLKs) (Marin 2006). Like MLKs, LRRK2 is a serine/threonine kinase with no detectable tyrosine kinase activity (West et al. 2007). Disease segregating mutations in LRRK2 have been reported in the kinase domain (G2019S, I2020T), the Roc domain (N1347H, R1441C/G), and in the COR domain (Y1699C) [reviewed in (Berwick et al. 2019)]. However, despite its relevance in PD, the physiological function of LRRK2 and the meaning of PD-linked mutations are yet to be completely understood. The protein inclusions observed in PD patients may be due to the failure of the protein clearance pathways. Intriguingly, experimental evidence suggests that LRRK2 might influence protein clearance acting on both the ubiquitin-proteosome system (Lichtenberg et al. 2011) and autophagy-lysosome pathway [reviewed in (Albanese, Novello, e Morari 2019)]. LRRK2 kinase activity plays a major role in LRRK2 physiological and pathological activity [reviewed in (M. Taylor e Alessi 2020)]. Few LRRK2 substrates have been characterized *in vivo*, including LRRK2 itself (Di Maio et al. 2018) and Rab proteins (Steger et al. 2016). In this study, we described that LRRK2 phosphorylates NSF *in vivo*. Mice expressing hLRRK2 G019S via BAC *(Melrose et al. 2010)* present an age-dependent motor and cognitive impairment together with deposition of NSF aggregates. At the mechanistic level, LRRK2 phosphorylation triggers the formation of NSF toxic aggregates.

Results

hG2019S mice show an age-dependent motor and cognitive impairment

Previous studies described an age-dependent neuropathological and behavioral phenotype in hG2019S BAC (hG2019S) mice (Melrose et al. 2010). We characterized age-matched wild-type and hG2019S male mice at 3, 6, 12 and 18-months in a battery of behavioral tests, including spontaneous motor activity (figure 1A-B), balance beam, pole test, rotarod (figure 1C-G) and novel object recognition (figure 1H). Three-months old wild-type and hG2019S cohorts performed equally in all experiments, except in the rotarod test at 32 rpm, where hG2019S mice were significantly impaired. Instead, while spontaneous activity did not differ between genotypes, we noticed an impairment in the motor performance at the balance beam and pole test at 6 months, in the rotarod (12 rpm) at 12 and 18 months, in the rotarod (32 rpm) at 6 and 18 months and in the rotarod resistance at 6 and 12 rpm. Finally, 6, 12 and 18 months old hG2019S mice scored significantly worse at the novel object recognition test in terms of mean discrimination index. These observations suggest that 6-months old hG2019S male mice show motor and cognitive impairment.

G2019S mutation correlates with the deposition of NSF aggregates

Protein aggregation is an established histological hallmark of PD. LC3 decorates LB in PD and DLB patients (Higashi et al. 2011; Tanji et al. 2011). Therefore we investigated the presence of proteinaceous aggregates in specimens from substantia nigra, striatum, cortex, and hippocampus obtained from 6-month old wild-type and hG2019S male mice via staining with LC3 antibody. Interestingly, we noticed the presence of a peculiar LC3 staining pattern in nigra, cortex, and hippocampus of hG2091S mice suggesting the presence of perinuclear pale bodies (supplementary figure 1). It has been suggested that LRRK2 mutations promote α-synuclein aggregation (Cresto et al. 2019; MacIsaac et al. 2020). Therefore we studied the distribution of α-synuclein in different brain areas of 6-month old wild-type and hG2019S mice. However, we did not report any overt α -synuclein deposition in hG2019S mice brain (supplementary figure 2A). LB (Xia et al. 2008) and the related intranuclear inclusion bodies (Pountney et al., 2008) contain more than 90 molecules, including NSF, which we described as LRRK2 functional partner (Piccoli et al. 2014; 2011). Consequently, we first analyzed the sub-cellular distribution of NSF in hG2019S cortical neurons. We noticed that NSF localizes in somatic structures positive for LC3 and p62 (figure 2A-B), i.e., resembling protein aggregates (Kopito 2000). Protein aggregates form high molecular weight (HMW) complexes that are retained by acetate cellulose in the filter retardation assay (Reid et al. 2003). We confirmed the presence of NSF HMW complex in the sample prepared from 6-months hG2019S mice brain (figure 2C-D) despite a similar expression of LRRK2 and NSF in the two mice lines (supplementary figure 3A-D). A well-established feature of protein aggregates is the resistance

to proteinase-K digestion (Kheterpal et al. 2001). Thus we characterized NSF aggregates by limited proteolysis in 6-months old wild-type and hG2019S male mice brain homogenates. Upon proteinase-K digestion, the 100 kDa MW band, corresponding to full length NSF protein, gradually disappeared in samples prepared from wild-type but not from hG2019S mice (figure 2E-F). Histological analysis revealed the presence of NSF positive aggregates in nigral, striatal, hippocampal, and cortical section prepared from 6-months hG2019S mice (figure 2G-H). Next, we characterized post-mortem basal ganglia specimen obtained from healthy control, idiopathic and G2019S PD cases. Detergent solubility profile characterizes proteinaceous aggregates from the biochemical standpoint (Mamais et al. 2013). Interestingly, while Triton-X100 soluble NSF levels were comparable among the groups (figure 3A, C), the yield of NSF in the SDS soluble fraction was higher in sample prepared from idiopathic or G2019S PD patients (figure 3B, D). More, we found that NSF decorates a proportion of α-synuclein positive structure in both idiopathic and G2019S PD cases (figure 3E and supplementary figure 3E). To directly assess the impact of G2019S mutation on the NSF aggregation state, we analysed dopaminergic neurons differentiated from G2019S human neuronal precursor and their respective gene-corrected line (supplementary figure 3F-G). By filter retardation assay, we noticed that NSF forms HMW complexes in samples prepared in G2019S dopaminergic neurons (figure 3F-G). Altogether this evidence suggests that LRRK2 G2019S mutation correlates with the deposition of NSF aggregates in both murine and human models.

LRRK2 G2019S kinase activity triggers NSF aggregation

We brought *in vitro* evidence that NSF is an LRRK2 substrate (Belluzzi et al. 2016). To complement this finding, we generated an antibody specifically recognizing NSF phosphorylated at Thr645 (supplementary figure 4A-B). This reagent showed that NSF phosphorylation at Thr645 increased in post-mortem samples gathered from G2019S patients specimen (figure 4A-C) and in several brain areas gathered from 6-months hG2019S mice (figure 4D-E). Structural analysis of NSF (PDB ID: 3J94) revealed that the side chain of T645 is close to the ATP-binding site on the D2 domain involved in NSF oligomerization (aa 490-744) (figure 4F-G). By differential detergent solubility assay, we noticed an increased amount of NSF in the insoluble fraction gathered from hG2019S cortical neurons (figure 4H-I). Surprisingly, such increase resulted resistant to chronic treatment with an LRRK2 kinase inhibitor. We obtained a similar outcome upon the overexpression of hLRRK2 G2019S in N2A cell (supplementary figure 4C-D). This biochemical evidence suggests that LRRK2 kinase activity triggers NSF aggregation. Proteins can aggregate upon impairment of proteasome activity (Varshavsky, 2017). Accordingly, a filter retardation assay showed that the pharmacological proteasome inhibition induced NSF aggregation in wild-type neurons. Instead, hG2019S neurons were characterized by a high basal amount of HMW NSF that did not further increase upon MG-132 treatment (supplementary figure 4E-F). Indeed, LRRK2 G2019S might interfere with UPS mediated NSF degradation. However, we reported a comparable UPS proteolytic activity in 6- or 12-months old wild-type and hG2019S mice (supplementary figure 4G). Therefore, we thought that other mechanisms must underline LRRK2 G2019S dependent NSF aggregation. Phosphorylation may directly affect protein folding and oligomeric state (Metskas e Rhoades 2015). To dissect the biological consequence of NSF phosphorylation on Thr645, we generated by site-

direct mutagenesis the NSF phosphomimetic variant NSF T645D. As expected (Belluzzi et al. 2016), NSF T645D has an augmented ATPase activity (supplementary figure 5A-B). NSF T645D is prone to aggregation independently from UPS blockade (supplementary figure 5C-D) and it forms higher-molecular weight complexes than the wild-type variant (supplementary figure 5E-F). NSF T645D is strongly enriched in the insoluble fraction, as suggested by differential detergent solubility (figure 4J-K). Strikingly, once co-expressed with HA-NSF wild-type, NSF T645D influenced the solubility of the wild-type protein (figure 4J, L). These observations suggest that phosphorylation at T645 triggers NSF aggregation. Once entrapped within aggregates, proteins get cleaved and tagged by ubiquitin (Olanow et al. 2004). Our western-blotting analysis revealed that NSF T645D undergoes proteolytic cleavage and is strongly decorated by ubiquitin (figure 4M-O). In ubiquitin chains, each monomer can be conjugated through different lysine residues, generating a code with functional consequences [reviewed in (Akutsu, Dikic, e Bremm 2016)]. To determine the nature of ubiquitination occurring on the two NSF variants, we expressed in HEK293 cells NSF WT and NSF T645D together with ubiquitin wild-type or with individual ubiquitin constructs missing lysine 48, 48 and 63 or 48, 63 and 29, respectively. We noticed that the degradation and the ubiquitination of the two NSF variants depend on different lysine residues (supplementary figure 5G-K). Altogether, these data suggest that LRRK2 phosphorylation at T645 alters NSF biochemical properties and promotes its aggregation.

NSF over-expression is detrimental for hG2019S neurons in an LRRK2 kinase dependent manner.

NSF plays a crucial role in neurons (Bonnycastle, Davenport, e Cousin 2020) . To investigate whether NSF aggregation may be neurotoxic, we infected wild-type and hG2019S neurons with lentiviral viruses expressing mCherry alone or together with NSF wild-type, the phospho-null variant NSF T645A or the phospho-mimetic variant NSF T645D. Neurons were treated from DIV10 to DIV14 with DMSO or GSK2578215A (GSK, 0.2 μM daily) and then processed at DIV16 (figure 5A and supplementary figure 6A). Neurite retraction is an established marker of neuronal damage (Chernova et al. 2007). Our morphological analyses revealed that the over-expression of either NSF wild-type or T645A had no major effect on wild-type neuron morphology. Instead, NSF T645D was detrimental to wild-type neurons. Noteworthy, NSF wild-type over-expression caused a significant reduction of neurite number in hG2019S neurons. Such morphological phenotype was absent in hG2019S neurons over-expressing the phospho-null NSF T645A variant (figure 5B). The analysis of neuronal viability via MTT assay confirmed this outcome (figure 5C). Interestingly, the chronic treatment with the LRRK2 kinase inhibitor GSK2578215A prevented the neurite loss of hG2019S cultures expressing wild-type NSF but did not ameliorate the overall viability. Cumulatively, these data indicate that NSF is neurotoxic upon LRRK2 phosphorylation.

Trehalose treatment clears NSF aggregates

Autophagy can attenuate protein aggregation (Fujikake, Shin, e Shimizu 2018). We used trehalose, a well-established autophagic inducer (DeBosch et al. 2016), to stimulate autophagy in wild-type and hG2019S neurons (supplementary figure 6B-C). The filter retardation assay suggested that trehalose treatment reduced NSF aggregation in NSF over-expressing HEK293 cell treated with MG132 (supplementary figure 6D-E). *In vivo*, trehalose treatment reduced NSF aggregation in 6-months old hG2019S male mice (1% in the drinking water, 1-month; supplementary figure 6F-G) without significant impact on animal weight (supplementary figure 6H). Specifically, trehalose treatment reduced the number of cells decorated by NSF in substantia nigra (figure 6), striatum (figure 7), cortex and hippocampus (figure 8) region of hG2019S mice. Caspase-3 cleavage

precedes the apoptotic cell death. We noticed a significant increase of cleaved-caspase 3 positive cells in nigra (figure 6) and striatum (figure 7) without any overt loss of TH density. Caspase-3 positive cells were also evident in the cortex and hippocampus (figure 8) of hG2019S mice. Trehalose treatment significantly reduced the number of caspase-3 positive cells in substantia nigra (figure 6), striatum (figure 7), cortex, and hippocampus (figure 8) of hG2019S mice. Our observations suggest that trehalose treatment cleared NSF aggregation and reduced cell death in hG2019S mice brain.

Trehalose treatment ameliorates motor and cognitive phenotype in hG2019S mice

Next, we profiled the motor and cognitive performances in 6-month old hG2019S and wild-type male mice upon chronic treatment with trehalose (figure 9). We reported a robust recovery of motor and cognitive abilities in trehalose-treated animals. In particular, trehalose treatment ameliorated the performances at the 6-mm balance beam (figure 9C), at the 32-rpm rotarod (figure 9F), the rotarod resistance at 12 rpm (figure 9G) and the novel object recognition (figure 9H). We also observed a partial improvement in motor and cognitive performances (in the rotarod 32 rpm and in the novel object recognition) in 12-month old hG2019S mice treated with trehalose starting at month 10 (1% in the drinking water, 2-month; supplementary figure 7). Altogether, these observations suggest that trehalose treatment is beneficial in rescuing behavioural defects of hG2019S mice.

Discussion

LRRK2 and the proteostatic control

In the present study we show that hG2019S mice present an age-dependent motor and cognitive impairment together with the deposition of protein aggregates containing NSF and signs of cell death in substantia nigra, striatum, cortex, and hippocampus. Post-mortem brain investigation demonstrated that LRRK2 G2019S patients often shows synucleinopathy, occasionally tauopathy, suggesting a role for LRRK2 in protein inclusion pathology (Taymans e Cookson 2010). The description of fronto-temporal ubiquitinated neuronal intranuclear inclusions in one patient carrying G2019S substitution indicates that LRRK2 pathological impact is not restricted to the substantia nigra (Dächsel et al. 2007; Kalia et al. 2015).

LRRK2 kinase activity brings to protein accumulation without affecting the catalytic activity of the proteasome or expression levels of proteasomal core subcomplexes (Lichtenberg et al. 2011). Instead, LRRK2 influences the autophagic pathways at multiple levels [reviewed in (Manzoni e Lewis 2017; Albanese, Novello, e Morari 2019; Cogo et al. 2020). The investigation of *LRRK2*-deficient mice revealed a biphasic alteration of autophagy in the kidney (Tong et al. 2010a; 2012); however, similar studies in an independent *LRRK2*-knock out mouse line demonstrated an

accumulation of secondary lysosomes in the kidney without major involvement of autophagy (Herzig et al. 2011a). Even more complicated is the state-of-art describing autophagy in an LRRK2 disease context. In fact, many authors conclude that G2019S mutation increases autophagy in different models, including stable cell lines (Gómez-Suaga et al. 2012; Plowey et al. 2008), fibroblasts (Yakhine-Diop et al., 2014), iPS derived neurons (Bravo-San Pedro et al. 2013), *C.Elegans* (Ferree et al., 2012) and mice (Ramonet et al., 2011). However, others studies have reported that the same mutation reduces (Manzoni et al. 2013) or at least does not affect (Sánchez-Danés et al. 2012; Wauters et al. 2019) autophagy. Such conflicting results leave unclear the impact of LRRK2 G2019S mutation on autophagy (Manzoni 2017). Still, increased accumulation of protein aggregates has been reported in complementary LRRK2 G2019S models (Bang et al. 2016; Guerreiro et al. 2016; Novello et al. 2018; Schapansky et al. 2018). Thus it might be possible that LRRK2 controls protein clearance acting upstream of the two main protein-clearance mechanisms.

Phosphorylation can trigger protein aggregation

Post-translational modifications regulate protein structure. In particular, phosphorylation can dictate protein folding and eventually, aggregation state. In the context of PD, phosphorylation has a severe impact on alpha-synuclein [reviewed in (Tenreiro, Eckermann, e Outeiro 2014)]. While soluble, monomeric alpha-synuclein is largely not phosphorylated in physiological conditions, up to 90% of LB-synuclein is phosphorylated on Ser-129 (Anderson et al. 2006). Indeed it is still unresolved whether phosphorylation might trigger or impair alpha-synuclein aggregation or toxicity. While a number of reports claim that phosphorylation at Ser-129 favours protein aggregation (Kragh et al. 2009; Wu et al. 2011) other authors described opposite or no effect (Fiske et al. 2011; Sancenon et al. 2012). However, phosphorylation at Ser-129 influences alpha-synuclein sub-cellular localization (Gonçalves e Outeiro 2013), suggesting that such PTM dictates alpha-synuclein function and fate. Similarly, hyperphosphorylated Tau protein precipitates in toxic aggregates and destabilizes the axonal tubulin cytoskeleton (Alonso et al. 2018). In vitro evidence shows that the phosphorylation of specific Tau residues modifies local folding, thus affecting global structure (Bibow et al. 2011; Inoue et al. 2012). We showed that LRRK2 phosphorylates NSF on Thr-645 *in vitro* (Belluzzi et al. 2016) as well as *in vivo* (here). Based on our structural analysis, the side chain of T645 falls in proximity to the ATP-binding site on NSF located on the D2 domain (aa 206-477). In particular, Thr-645 lies very close to the phosphate group of the bound ATP molecule. ATP binding on the D2 domain is essential for the formation of NSF hexamer (Whiteheart, Schraw, e Matveeva 2001). We determined by complementary means that upon phosphorylation at Thr-645 NSF forms *bona fide* HMW aggregates, being insoluble to Triton-X100 (Naslavsky et al. 1997), resistant to proteinase-K treatment (Kheterpal et al., 2001) and decorated by ubiquitin and p62 (Bjørkøy et al. 2005).

Altogether, our data suggest that the phosphorylation of NSF at T645 promotes NSF oligomerization and eventually triggers its precipitation into protein inclusions. Indeed it is unlikely that LRRK2-mediated phosphorylation is sufficient by itself to cause NSF aggregation. We reported that Rab3A, a well-established LRRK2 substrate (Lis et al. 2018; Steger et al. 2016), does not aggregate in BAC hG2019S mice (supplementary figure 2B). Thus, LRRK2 phosphorylation might not be the unique driver promoting NSF aggregation. Actually, in idiopathic PD patients we noticed that NSF is expressed at high level and decorates a proportion of LB. This evidence may argue against a causative role for LRRK2 kinase activity. However, it has been recently postulated a role for LRRK2 in idiopathic patients (Di Maio et al. 2018). It is tempting to speculate that in presence of increased NSF level even the low kinase activity characterizing wild-type LRRK2 may be sufficient to promote NSF aggregation. As reported for other aggregation-prone proteins like tau, it is conceivable that NSF has an intrinsic propensity towards aggregation that is pathologically exacerbated upon LRRK2 phosphorylation.

NSF aggregation, ageing, and neuronal toxicity

NSF is a key component of presynaptic machinery, allowing the first step of SV recycling (Pallanck et al. 1995). Numerous studies have shown that depletion of cytosolic NSF impair membrane fusion machinery (Rothman, 1994) and results in the accumulation of intracellular vesicles (Malhotra et al. 1988; Mohtashami et al. 2001). Thus, NSF aggregation might affect presynaptic fusion machinery. Interestingly, it has been reported that experimental ischemia induces NSF aggregation into Triton-X100 insoluble inclusions that harm neuronal function via sequestering synaptic vesicle (Liu e Hu 2004). A presynaptic dysfunction might indeed explain the early-stage manifestation of PD observed in animal models (Longo et al. 2017; Melrose et al. 2010; Sloan et al. 2016) or in presymptomatic LRRK2 G2019S carriers (Sossi et al. 2010). However, it is difficult to envisage how aberrant vesicle release could cause the overt neuronal death that characterizes the late phase of the disease. Neurons benefit from several pathways to effectively handle protein aggregation, but the ultimate resource to counteract proteinaceous stress is the degradative clearance of misfolded protein (Rubinsztein 2006). Nonetheless, the structure of the proteasome complex itself disfavours the removal of large oligomeric and aggregated proteins: substrates need to be unfolded to pass through the tight pore of the proteasome barrel (Verhoef et al. 2002). Autophagy may help, being capable of handling large protein aggregates (Hara et al. 2006; Komatsu et al. 2006). Unfortunately, both autophagy and proteasome activity pronouncedly declines with ageing (Del Roso et al. 2003; Graham e Liu 2017; Martinez-Vicente, Sovak, e Cuervo 2005). Thus, ageing and pathological LRRK2 phosphorylation together may contribute to the deposition of NSF aggregates. Given the low stoichiometry that we reported for LRRK2-driven NSF phosphorylation *in vitro*

(Belluzzi et al. 2016), it may well be that NSF phosphorylation occurs rarely *in vivo*. However, we noticed that T465D NSF affects the detergent solubility of the unmodified protein. Thus, we may depict a model where few phosphorylated NSF molecules lead the formation of pathological seeds capable of sequestering unphosphorylated protein into large aggregates that accumulate along with ageing.

Hints toward a therapy

Altogether this evidence may call for a therapeutic strategy targeting LRRK2 kinase activity. Several brain penetrant LRRK2 selective inhibitors have been identified [reviewed in (Ding e Ren 2020)]; however the broad expression of LRRK2 in other organs apart from the central nervous system, including lung, kidney and the immune system raise issues about side effects (Baptista et al. 2013; Fuji et al. 2015; Herzig et al. 2011b; Ness et al. 2013; Tong et al. 2010b; Baptista et al. 2020). In our model, LRRK2 kinase inhibition resulted partially toxic and not efficacious in resolving NSF aggregation. Thus, complementary therapeutic approaches are still needed. Targeting the protein aggregates caused by LRRK2 kinase activity may be clinically relevant. It is reasonable to predict that LRRK2 kinase activity affects the biochemical profile of other substrates besides NSF. Thus, a more holistic solution is needed. The activation of autophagy may promote the clearance of toxic protein aggregates. We report that chronic treatment with trehalose reduced NSF aggregation and ameliorated motor and cognitive phenotype in aged G2019S mice. Treatment with trehalose already demonstrated to be protective in models of Huntington disease, spinocerebellar ataxia, MAchado-Joseph disease, and Parkin-PD (Rodríguez-Navarro et al. 2010; Sarkar et al. 2007; Seki et al. 2010; Zaltzman et al. 2020). However, the pharmacokinetics properties of trehalose are poor. Small intestine, kidney and CNS expression of trehalose catalytic enzyme, trehalase, limits its bio-availability (Halbe e Rami 2019). Also, dietary trehalose results in digestive issues (Montalto et al. 2013) and may enhance the virulence of common nosocomial pathogen (Collins et al. 2018). These issues severely reduce the possibility of introducing trehalose into the clinical management of PD patients. In conclusion, boosting autophagy may be a powerful therapeutic strategy in LRRK2-PD, but a clinically relevant drug is still to be discovered.

Experimental procedures

Animals.

All animal protocols were approved by the University of Trento and National Ministery of Health (IACUC 793/2016-PR). The murine *G2019S-LRRK2* BAC mice were previously described (Li et al., 2010) and have been backcrossed onto the C57BL/6J mice for >10 generations.

Animals were kept in a normal light/dark cycle (12 hours light/ 12 hours dark) and had free access to food and water. All procedures involving animals were approved by Institutional agencies (OPBA- Università degli Studi di Trento) and Italian Ministry of Health (Università degli Studi di Trento prot. n. 793/2016-PR).At 5 or 10 months, Wild-type and *G2019S-LRRK2* BAC male littermates were divided into trehalose and control groups. In the trehalose group, mice were offered 1% trehalose drinking water solution. The treatment solution was changed every week. In the control group, mice were given drinking water. Mice body weight was measured every week since the start of treatment. Only male mice were used in our experiments due to a strong gender effect (Pischedda et al., manuscript in preparation).

Assays in post-mortem specimen

In total, 5 idiopathic, 4 G2019S and 5 control human brain cases were used in the study which were obtained from the archives of QSBB following appropriate local ethics committee approval. Demographic details of the cases have been described previously (Mamais et al. 2013).

For biochemical analysis, 5µg of TBS soluble fraction and 10µg from TBS-5% SDS fractions of basal ganglia homogenates were run on 10% Bis-tris gels with MOPS as running buffer. Details of homogenisation and fractionation procedure is mentioned in a previous publication (Mamais et al 2013). Protein from gels were transferred onto PVDF membranes and probed with NSF (SYSY, mouse monoclonal) and beta actin (Sigma, mouse monoclonal) antibodies overnight with shaking. Following incubation with appropriate HRP conjugated secondary antibodies, blots were visualized by enhanced chemiluminescence (Pierce; UK) detection. Protein expression levels were determined by densitometry and NSF results normalised to beta-actin levels. For immunohistochemical evaluation, 8µm substantia nigra sections from control, 4 iPD and 2 G2019S-LRRK2 PD were dewaxed in xylene, and pre-treated with 95% formic acid for 10min to expose antigenic sites. Standard immunohistochemistry protocol was followed using NSF (1:200 mouse monoclonal; SY-SY) and alpha-synuclein (1: 300; rabbit polyclonal, Abcam) primary antibodies with o/n incubation at 4C. Double immunofluorescence was performed using tetramethyl rhodamine labelled secondary antibody for alpha-synuclein and NSF with the fluorescein signal amplification kit (Perkin Elmer, UK). Following adequate washes to remove background fluorescence, sections were mounted with Aquamount (Merck, UK). Control sections where primary antibody was omitted displayed no significant background staining. Fluorescent signals from sections were scanned using Leica fluorescent microscope (Leica CTR6000). Total alpha-synuclein positive LBs were counted from each section and the proportion of NSF+ve LBs were derived. Human brains were donated to the Queen Square Brain bank for neurological disorders, UCL Queen Square Institute of Neurology and stored under a research license No:12198.

Behavioural tests

Spontaneous Motor Activity. Spontaneous motor activity was evaluated in an automated activity cage (43 cm × 43 cm × 32 cm) (Ugo Basile,Varese,Italy) placed in a sound-attenuating room as previously described (Ferri et al. 2004).Cumulative horizontal and vertical beam breaks were counted for 3 hours.

Balance Beam walking. The beam apparatus consists of 1 meter beams with a flat surface of 12 mm or 6 mm width resting 50 cm above the table top on two poles according to (Luong et al. 2011). A black box is placed at the end of the beam as the finish point. Nesting material from home cage is placed in the black box to attract the mouse to the finish point. A lamp (with 60 watt light bulb) is used to shine light above the start point and serves as an aversive stimulus. A video camera is set on a tripod to record the performance. On training days, each mouse crosses the 12 mm beam 3 times and then the 6 mm beam 3 times. The time required to cross to the escape box at the other end (80 cm away) is measured with a stopwatch. The stopwatch is started by the nose of the mouse entering the center 80 cm, and stopped when the animal reaches the end of the 80 cm. Once the mice are in the safe box, they are allowed some time (~15 secs) to rest there before the next trial. The mice rest for 10 min in their home cages between training sessions on the two beams. On the test day, the time to cross each beam is recorded. The beams and box are cleaned of mouse droppings and wiped with towels soaked with 70% ethanol and then water before the next beam is placed on the apparatus.

Pole test. In the vertical pole task, the mouse was placed on a vertical wire-mesh pole with its head facing upwards. Mice were habituated to the task in 2 trials per day for 2 days. On test day (third day) mice were subjected to 5 trials: the total time taken to turn the body and to descend was recorded according to (Hickey et al. 2008). A cut-off of 60 sec was given. Data were shown as mean of 5 trials evaluated during the test day.

Rotarod. The rotarod apparatus (Ugo Basile, Biological Research Apparatus, Varese, Italy) was used to measure fore and hindlimb motor coordination and balance (Dauge et al. 2001). During the training period, each mouse was placed on the rotarod at a constant speed (12 or 32 rpm) for a maximum of 120 sec, and the latency (sec) to fall off the rotarod, within this time period, was recorded. Mice received four tests/trial each day for 4 consecutive days. The fourth test of each trial was evaluated for statistical analysis**.** The fifth day mice were submitted to Rotarod resistance at a constant speed (12 rpm) for a maximum of 30 min and the latency (sec) to fall was measured.

Novel object recognition. The novel-object recognition test was performed over a 3-day period in an open plastic arena (60 cm x 50 cm x 30 cm), as previously described (Pan et al. 2008). Animals

were habituated to the test arena for 10 min on the first day. After 1 day habituation, mice were subjected to familiarization (T1) and novel-object recognition (T2). During the initial familiarization stage, two identical objects were placed in the centre of the arena equidistant from the walls and from each other. Each mouse was placed in the centre of the arena between the two objects for 20 min or until it had completed 30 s of cumulative object exploration. Object recognition was scored when the animal was within 0.5 cm of an object with its nose toward the object. Exploration was not scored if a mouse reared above the object with its nose in the air or climbed on an object. Mice were returned to the home cage after familiarization and then tested again after different delays (from 5 min to 24 h later). A novel object (never seen before) took the place of one of the two familiars. Scoring of object recognition was performed in the same manner as during the familiarization phase. From mouse to mouse the role (familiar or new object) as well as the relative position of the two objects were counterbalanced and randomly permuted. The objects for mice to discriminate consisted of white plastic cylinders and coloured plastic Lego stacks of different shapes. The arena was cleaned with 70% ethanol after each trial. An experimenter blind to the genotype group manually recorded the exploration times to the objects for each animal. Total time spent exploring the two objects during T1 and T2 was also calculated.

Cell cultures

Neuron cultures were prepared from mouse cortexes obtained from embryonic day 15.5–16.5 wild-type or hG2019S mice (C57BL/6J) as previously reported (Pischedda e Piccoli 2015; Pischedda et al. 2018). Briefly, after brain dissection the cortexes were mechanically dissociated after 15 min incubation with 2,5% Trypsin (Euroclone) at 37 °C in agitation. The resulting cells were counted and cryopreserved or directly plated on previously poly-D-lysine (Sigma) coated wells or cover slips, according to the desired density. High density (750–1000 cells/mm2) neuron cultures were plated on 12-well plastic tissue culture plates (Iwaki; Bibby Sterilin Staffordshire, UK) and medium-density (150–200 cells/mm2) onto 12mm diameter cover slips inserted into 24-well plastic tissue culture plates (Iwaki). The cells were grown in Neurobasal at 37°C and 5% CO_2. Neuronal transfection was carried out using Lipofectamine 2000 (Life Technologies) following the manufacture’s instruction. The cells were treated with LRRK2 kinase inhibitor, GSK-2578215A (Tocris Bioscience, Bristol, UK), MG132 (Tocris Bioscience, Bristol, UK) and Trehalose (Sigma) by addition to culture media at the concentrations indicated through the text.

Human embryonic kidney cells (HEK293T) were cultured in DMEM complete: Dulbecco's modified Eagle's medium (DMEM, Euroclone) supplemented with 10% fetal bovine serum (FBS, Euroclone) at 37°C and 5% CO2. HEK293T were transiently transfected using linear polyethylenimine (PEI, Polysciences) with ratio DNA: PEI 0.8:100. 4 µg of DNA were dissolved in

0.5 ml of PEI solution and vortexed for 20 sec. The DNA-PEI mix was incubated for 10 minutes at room temperature (RT) and added directly to the cells. The medium was changed after 24h and the cells were lysed 48h post transfection. Lentiviruses were produced by transient transfection of HEK293T cells according to standard protocols (Wiznerowicz e Trono 2003). Primary cortical cultures were transduced at DIV4 with lentiviruses at multiplicity of infection 3 (MOI3). The 3-(4,5-dimethylthiazol-2-yl)-2,5-diphenyltetrazolium bromide (MTT) assay was performed to measure culture viability as described (Mosmann 1983). High density (750–1000 cells/mm2) neuronal culture were infected at DIV 4 and processed for MTT assay at DIV16. Briefly, MTT ((3-(4, 5-dimethylthiazolyl-2)-2, 5-diphenyltetrazolium bromide- Sigma Aldrich) stock solution 20X (5mg/ml in MilliQ water) was diluted in neuronal complete media and cells were were incubated with MTT mix for 30 minutes at 37°C with 5% CO2. After incubation, media was discarded, cells were resuspended in DMSO to dissolve the intracellular purple precipitates and the absorbance was measured at 570 nm with the Plate reader Infinite 200 PRO (Tecan Life Sciences). Toxicity was calculated as 1- cell viability, being cell viability expressed as fold over control.

iDA culture

Wild-type, G2019S and G2019S corrected Human iPSCs derived Neuronal Precursors Cells (NPCs) were obtained from Dr. Deleidi lab and cultured as previously reported (Reinhardt et al. 2013). Briefly, the cells were expanded in 50:50 DMEM F12 and Neurobasal medium with: 1% P/S, 1% B27 (without Ascorbic acid), 0,5% N2, 1%L-glutamax, 150 µM Ascorbic acid, 3 µM CHIR, 0.5 µM Purmorphamine (PMA) (NPC expansion medium). Media was changed every other day and cells were passed every week after 10 min incubation with Accutase (200ul/12 well). The cells were re-plated at a 1:10 ratio in 12-well plates pre-coated with Matrigel (1:30 from Stock) in 'NPC expansion medium' supplemented with 10 µM ROCK inhibitor for the first day after splitting. After the second passage, when the cells reached 80% of confluency, the media was changed to Ventral CNS differentiation medium (50:50 DMEM F12 and Neurobasal medium with: 1% P/S, 1% B27 (without Ascorbic acid), 0,5% N2, 1%L-glutamax, 100 ng/mL FGF8, 200 µM of Ascorbic acid and 1µM PMA. When confluent the cells were split with Acutase and re-plated in Matrigel coated 6 wells plate at a 1:1 ratio. The media was changed every other day. After 10 days the Ventral CNS differentiation medium I was changed to maturation medium (50:50 DMEM F12 and Neurobasal medium with: 1% P/S, 1% B27 (without Ascorbic acid), 0,5% N2, 1%L-glutamax, 10 ng/mL BDNF, 10 ng/mL GDNF, 1ng/mL TGF-b3, 200 µM ascorbic acid, 500 µM dbcAMP and 0,5 µM PMA). After 48h the media was changed to dopaminergic differentiation medium (50:50 DMEM F12 and Neurobasal medium with: 1% P/S, 1% B27 (without Ascorbic acid), 0,5% N2, 1%L-glutamax, 10 ng/mL BDNF, 10 ng/mL GDNF, 1ng/mL TGF-b3, 200 µM ascorbic acid, 500 µM

dbcAMP). The cells were kept in dopaminergic differentiation medium until the end of the experiment and the medium was changed every 2-3 days.

Immunohistochemistry

Six and 12 months old mice were anaesthetized and transcardially perfused with PBS 1X followed by 4% paraformaldehyde in PBS 1X. Brains were dissected, postfixed for 2h by immersion in the same fixative and then cryoprotected by immersion in 30% sucrose solution in PBS 1X for 24 h at 4°C. Brains were included in OCT and stored at -80°C until processing. 14 µm brain coronal sections were obtained after serial sectioning on Leica cryostat and mounted on Polysine Slides (Thermo Fischer Scientific). The slices were saturated in 2,5% BSA, 10% NGS, 0,2% Triton X-100, PBS 1X, for 1 hour at RT and incubated with the primary antibody O/N at 4°C. After 3 washes in PBS 1X – 0,2% Triton X-100 the sections were quenched for 15 min in PBS 1X plus 0,3% H_2O_2at RT, then washed with PBS 1X. The sections were incubated for 30 min with the secondary biotinylated antibody at RT. The slices were then rinsed in PBS1X and incubated for 30 minutes with Vectastain ABC kit 1:1 mix (Vectorlab), washed 2 times in PBS 1X – 0.2% Triton X-100, washed once in PBS1X, and developed with DAB quanto mix (Thermo Scientific) for 30 sec. The stained sections were rinsed in PBS 1X stained in Hematoxylin solution, Gill No.2 (Sigma Aldrich) for 2,5 minutes and then washed for 2 minutes with tap water. Sections were incubated with differentiation solution (70% ETOH plus 0,3% HCl) for 10 seconds, washed with tap water and then incubated for 30 seconds with Scott's Tap water Substitute (Sigma Aldrich) for blueing. Sections were then dehydrated, mounted using DPC mounting reagent (Sigma) and kept at RT until acquisition with a Zeiss Axio Imager M2 equipped with 40X objective.

Immunofluorescence

For the immunostaining experiments, neurons were fixed in 4% paraformaldehyde and 4% sucrose at room temperature or 100% methanol at -20°C. mCherry positive neurons were randomly chosen for quantification in at least four independent experiments for each condition. Cover slips were mounted with prolonged reagent (Life Technologies) and observed with Zeiss Observer Z1 microscope equipped with an Apotome module. The obtained images provide an axial resolution comparable to confocal microscopy(Garini, Vermolen, e Young 2005; Schaefer, Schuster, e Schaffer 2004). Images were acquired with AxioObserv Z1 microscope equipped with Apotome module using a plan-Apochromat 63x/1.40 Oil objective, pixel size 0,102 mm x 0.102 mm. Acquired images were analyzed with ImageJ software using NeuronJ plugin (Meijering et al. 2004).

Polyclonal phospho-specific NSF antibody production and purification

Affinity-purified anti-P-Thr645-NSF polyclonal antibody was made in a NZW female rabbit (Envigo) by immunization against a single peptide (amino acids 631–656: KKAPPQGRKLLIIGpTTSRKDVLQEME), encompassing the LRRK2 phosphorylation site of NSF, conjugated via an N-terminal Cys residue to maleimide-activated KLH (keyhole limpet haemocyanin, Sigma-Aldrich). Rabbit was injected subcutaneously four times at 3-week intervals, with 0.5 mg of phosphopeptide-protein conjugates in PBS emulsified with Freund's adjuvant (1:1 v/v). After the last immunization, blood was collected and antisera was purified using an immobilized peptide affinity resin (Sulfo Link Coupling Gel, Thermo) according to manufacturer's instructions. Briefly, a shorter peptide (LIIGpTTSRKD) was conjugated via an N-terminal Cys residue and coupled to the resin. Fractions were eluted with Glycine Buffer (0.2 M, pH 2.5) into Tris buffer (1 M, pH 8.5) solution for pH neutralization. Protein eluted fractions (as determined by Abs at 280 nm) were pooled and concentrated by ultrafiltration (Amicon Ultra-15 30KD, Millipore). All synthetic peptides were synthesized, purified by RP-HPLC, and confirmed by mass spectroscopy at CRIBI (University of Padova) as previously described (Ottaviani et al. 2017). All animal protocols were approved by the University of Padova and National Ministery of Health (IACUC 906/2016-PR).

Biochemical assays

Proteinase K digestion. Proteinase K digestion of mouse brain lysates was performed on samples prepared from 6 months mouse LRRK2 wild-type and LRRK2 G2019S brains. Brains were solubilized by mechanical homogenization of 1g of tissue in lysis buffer (150 mM NaCl, 2 mM EDTA, 50mM Tris-HCl, 1% NP-40 and 0.25% sodium deoxycholate, pH 7.4) using a pestle and incubated 1h at 4ºC. Next brain lysates were centrifuged at 14,000xg for 10 min at 4°C to collect supernatant and samples were quantified following Bradford's method. Proteinase K was added to 50 µL of sample (previously prepared at 1µg/µL concentration) at different final concentration ranging from 0.3-0.5 µg/mL and incubated at 37ºC for 25 minutes under shaking. Digestion reactions were stopped by addition of the inhibitor PMSF (4mM) and samples (undigested and exposed to Proteinase K) were prepared in sample buffer 5X for Western-blotting analysis.

Proteasome activity. Proteasome activity in mice brain tissue was analysed following the 20S Proteasome activity assay kit protocol by Millipore (APT280). The assay detects the fluorophore 7-Amino-4-methylcoumarin (AMC) after cleavage from the labelled substrate LLVY-AMC. Briefly, 3 µg of protein from each sample was incubated for 1 h at 37°C with proteasome labeled substrate in 96 dark multiwells. The sensibility of the assay was tested performing serial dilution of proteasome positive control (1:4 to 1:256) of the stock solution in 1X Assay buffer. Fluorescence data was

collected using a PE Biosystems CytoFluor 400 plate reader using a 380 nm excitation and 460nm emission filters.

Filter retardation assay. Filter retardation assay were performed as described in (Perez Carrion et al. 2018). Briefly, cell cultures were rinsed once in cold PBS 1X and mechanically detached in PBS 1 X plus protease and phosphatase inhibitor cocktails Calbiochem (40 µl/well 12 wells plate). Cell samples were sonicated 3 times with 1s pulse and 1s stop sequence at 10% pulse amplitude. Brain extracts from 6 months mouse LRRK2 wild-type and LRRK2 G2019S variant were prepared by mechanical homogenization of 1 gr of tissue in solubilization buffer (150 mM NaCl, 2 mM EDTA, 50mM Tris-HCl, pH 7.4) using a pestle and incubated 1h at 4ºC. Then brain lysates were centrifuged at 14,000xg for 10 min at 4°C to collect supernatant. Protein amounts were quantified following Bradford's method. Ten µg of each sample were diluted to 120 µl in PBS 1X. The samples were immobilized on methanol equilibrated cellulose acetate membrane through a dot blot void system (BioRad).

Streptavidin pull down. Streptavidin pull down was performed as described in (Pischedda et al. 2014). Briefly, HEK293T cells were transiently transfected and treated as indicated trough the text. The cells were then resuspended in 5ml ice cold PBS 1X, centrifuged at 150xg for 5 min and lysed in 1 ml of 50mM HEPES pH 7.4, 150mM NaCl, 0.5mM EDTA, 0.5% Triton X-100, protease inhibitors (Calbiochem) and phosphatase inhibitor cocktails II and IV (Calbiochem), after incubation for 1 h at 4°C in rotation. The cell lysate was recovered after 10 min centrifugation at 15000xg at 4°C and 10% of supernatant kept as input. The remaining supernatant was incubated with 25 µl of Streptavidin resin (IBA) for 1 hour at 4°C in rotation. After three washes in 0.5 ml of 50mM HEPES pH 7.4, 150mM NaCl, 0,2% Triton X-100, the bound protein was eluted in 60 µl of Laemmli buffer 1X after 10 min incubation at 52°C.

Solubility assay. HEK293T cells were cultivated in 12 well plates and transiently transfected and treated as indicated trough the text. Cells were rinsed with cold PBS1X and then lysed in Triton-X100 buffer at 4°C (50mM HEPES pH 7.4, 150mM NaCl, 1 % Triton X-100, protease inhibitors (Calbiochem) and phosphatase inhibitor cocktails II and IV (Calbiochem)). The cell lysate was kept on ice and briefly vortexed every 10 minutes for 3 times, then centrifuged at 16.000g for 10 minutes at 4°C. The Supernatant was collected as the detergent-soluble fraction and the pellet constituted the insoluble fraction. The pellet was resuspended in 75 ul of Laemmli sample buffer 2X, whereas the same volume of Laemmli sample buffer 5X was added to the soluble fraction.

Protein purification. HEK-293T cells were lysed in lysis buffer [20 mM Tris–HCl, pH 7.5, 150 mM NaCl, 1 mM EDTA, 2.5 mM Na4P2O7, 1 mM beta-glycerophosphate, 1mM NaVO4, Protease Inhibitor Mixture (Sigma-Aldrich)] by using a needle. Cleared lysates (1 ml) were incubated with 30 µl of anti-FLAG-M2-agarose beads by rotating overnight at 4°C. Resin complexes were washed

with different buffers WB1 (20mM Tris–HCl pH7.5, 500mM NaCl) twice, WB2 (20mM Tris–HCl pH7.5, 350mM NaCl) twice, WB3 (20mM Tris–HCl pH7.5, 150mM NaCl) six times. Proteins were eluted in WB3 with 150 ng/µl of 3× FLAG peptide) for 30 min at 4°C with shaking. Purified proteins were resolved by SDS–PAGE and stained with Coomassie Brilliant Blue to verify protein purity. Protein content was calculated by densitometry, using a standard curve with bovine serum albumin (BSA).

ATPase assay. NSF ATPase activity was quantified using the Malachite Green Assay by measuring the release of inorganic phosphate (Pi) due to the ATP hydrolysis with spectrophotometer as previously described (Belluzzi et al. 2016). 216 nM NSF was incubated with different ATP concentrations and 2 mM MgCl2 for 2h a 37°C. The samples were mixed with Malachite Green stock solution and the absorbance measured at 640nm. The values of absorbance were then converted into µmol of free Pi in solution using a standard curve. Kinetic constants were obtained by data fitting with the Michaelis-Menten kinetic model Y = Vmax*S/(Km + [S]).

Size Exclusion Chromatography (SEC) and dot blot analysis. SEC was performed as previously described (Belluzzi et al. 2016). Briefly, Strep-FLAG NSF WT and T465D transfected HEK-293T cells were lysed in 0.5ml of lysis buffer containing 0.06% (v/v) Triton X-100 and centrifuged. Cell lysates were separated on a Superose 6 10/300 column (Ge Healthcare, Waukesha, WI, USA) pre-equilibrated with 20mM Tris–HCl pH7.5, 150mM NaCl and 0.06% (v/v) Triton X-100. The flow rate used was 0.5ml/min. Fractions of 0.25ml were collected and spotted onto a nitrocellulose membrane and analyzed by dot blot. Densitometric analysis was performed by using ImageJ program.

Western-blotting. Protein samples were resolved on to 10-15% Tris-glycine polyacrylamide gels in SDS/Tris-glycine running buffer. Solubilized proteins were transferred to nitrocellulose or polyvinylidenedifluoride (PVDF) membranes in blotting buffer containing 10% methanol. The membrane was saturated for 1 h at RT in 5% nonfat dry milk in Tris-buffered saline and 0.1% Triton (TBS-T) and then incubated with the primary antibody in saturating solution for 90 min at RT. The unbound primary antibody was sheets was washed out in TBS-T (3x10 min) at RT and the membrane was incubated for 1 h at RT with horseradish peroxidase-conjugated anti-mouse or anti-rabbit IgGs. After 3 washes in TBS-T 10 min/each at RT, the immunoreactive proteins were visualized using enhanced chemioluminescence plus (ECL+, GE Healthcare, Little Chalfont, England). Densitometric analysis was carried out using Image J software.

Structure analysis. The Cryo-EM structure of NSF hexamer was downloaded from the PDB database, and the structural analysis was performed using the program PyMOL (*http://www.pymol.org/*). All the structural diagrams were prepared using the program PyMOL.

Statistical analysis and guidelines

All data are expressed as mean ± standard error of the mean (S.E.). The normality of data distributions was determined using the D'Agostino and Pearson omnibus normality test, followed by an unpaired Student's t test, ANOVA followed by Tuckey's post-hoc test or two-way ANOVA followed by Bonferroni or Student's t post-hoc test as appropriate. The indication of number of experiment (n) and level of significance (p) are indicated throughout the text. All methods were performed in accordance with the relevant guidelines and national regulations.

List of expressing vectors

HA- Ubiquitin (pcDNA3.1), HA- K48R Ubiquitin (pcDNA3.1); HA- K63R Ubiquitin (pcDNA3.1) HA- K29,48,63R Ubiquitin (pcDNA3.1) (kind gifts by Dr. Simona Polo, IFOM);

LRRK2 K1906M GFP (pcDNA3.1), LRRK2 G2019 GFP (pcDNA3.1) [described in (Gloeckner et al. 2006);

Strep-FLAG hNSF WT (pcDNA3.1), Strep-FLAG hNSF T645A (pcDNA3.1) [described in (Belluzzi et al. 2016)], Strep-FLAG hNSF T645DE (pcDNA3.1) and Strep-FLAG hNSF T645D (pcDNA3.1) generated by site directed mutagenesis;

HA hNSF (pCMV HA-2) (kind gift by prof. Dario Alessi);

Strep-FLAG hNSF WT (pULTRA HOT) and Strep-FLAG hNSF T645D (pULTRA HOT) generated via cloning into NheI-BclI sites

List of primary antibodies

NSF (123 002-Synaptic System); alpha-Synuclein (D37A6- Cell Signaling); LC3 (NB100-2331- Novus Biologicals); p62 (ab109012- ABCAM); b-ACTIN (sc-47778 – Santa Cruz Biotechnology); FLAG (sc-166355- Santa Cruz Biotechnology); HA (Cat. #05-904- Merck Millipore); cleaved-caspase-3 (9H19L2- Invitrogen); TH (AB152- Merck Millipore); b3- Tubulin (ab18207- ABCAM); Synapsin-1 (D12G5- Cell Signaling); RAB 3a (107 111- Synaptic System); LRRK2 phospho S935 (UDD2 10(12) ab133450 – ABCAM); LRRK2 (MJFF2 (c41-2) ab133474 – ABCAM); LRRK2 phospho S1292 (MJFR-19-7-8 ab203181 – ABCAM)

List of secondary antibodies

Anti Rabbit IgG (H+L), made in goat, Biotinylated (BA-1000- Vector Laboratories); Anti Mouse IgG (H+L), made in horse, Biotinylated (BA-2000- Vector Laboratories)**;** Alexa Fluor® 488 AffiniPure Goat Anti-Rabbit IgG (H+L) (111-545-144 - Jackson ImmunoResearch); Goat IgG anti-Rabbit IgG (H+L)-TRITC (111-025-003 - Jackson ImmunoResearch); Peroxidase AffiniPure Goat

Anti-Mouse IgG (H+L) (115-035-146 - Jackson ImmunoResearch); Peroxidase AffiniPure Goat Anti-Rabbit IgG (H+L) (115-035-003 - Jackson ImmunoResearch)

Author Contributions

F.P., M.D.C, L.P., A.B. M.P.C., G.S., M.S. performed experiments, M.M., Li.P., E.G., O.M., R.B., M.E.S., G.P. analysed data and wrote the paper.

Acknowledgments

G.P. is supported by Fondazione Telethon (grant TDPG00514TA), MIUR (PRIN-2017ENN4FY), and Fondazione Cariplo (project 2019-3415). F.P. received support by Fondazione Caritro (project 2019.0230). This work was supported by Fondazione Cariplo (grant 2011-0540) to G.P. and E.G. and Fondazione Telethon (grant GGP12237) to G.P., E.G. and M.M. G.P. is grateful to the Michael J. Fox Foundation, the FIRB program (grant RBFR08F82X_002) and Fondazione Grigioni per il morbo di Parkinson. We gratefully thank Prof. Matthew Farrer and Dr. Heather Melrose for providing LRRK2 hG2019S BAC mice, to Marzia Indrigo for excellent technical advice and Giuseppe La Tona for support in animal handling.

Akutsu, Masato, Ivan Dikic, e Anja Bremm. 2016. «Ubiquitin Chain Diversity at a Glance». *Journal of Cell Science* 129 (5): 875–80. https://doi.org/10.1242/jcs.183954.

Albanese, Federica, Salvatore Novello, e Michele Morari. 2019. «Autophagy and LRRK2 in the Aging Brain». *Frontiers in Neuroscience* 13: 1352. https://doi.org/10.3389/fnins.2019.01352.

Alonso, Alejandra D., Leah S. Cohen, Christopher Corbo, Viktoriya Morozova, Abdeslem ElIdrissi, Greg Phillips, e Frida E. Kleiman. 2018. «Hyperphosphorylation of Tau Associates With Changes in Its Function Beyond Microtubule Stability». *Frontiers in Cellular Neuroscience* 12: 338. https://doi.org/10.3389/fncel.2018.00338.

Anderson, John P., Donald E. Walker, Jason M. Goldstein, Rian de Laat, Kelly Banducci, Russell J. Caccavello, Robin Barbour, et al. 2006. «Phosphorylation of Ser-129 Is the Dominant Pathological Modification of Alpha-Synuclein in Familial and Sporadic Lewy Body Disease». *The Journal of Biological Chemistry* 281 (40): 29739–52. https://doi.org/10.1074/jbc.M600933200.

Bang, Yeojin, Kwang-Soo Kim, Wongi Seol, e Hyun Jin Choi. 2016. «LRRK2 Interferes with Aggresome Formation for Autophagic Clearance». *Molecular and Cellular Neurosciences* 75: 71–80. https://doi.org/10.1016/j.mcn.2016.06.007.

Baptista, Marco A. S., Kuldip D. Dave, Mark A. Frasier, Todd B. Sherer, Melanie Greeley, Melissa J. Beck, Julie S. Varsho, et al. 2013. «Loss of Leucine-Rich Repeat Kinase 2 (LRRK2) in Rats Leads to Progressive Abnormal Phenotypes in Peripheral Organs». *PloS One* 8 (11): e80705. https://doi.org/10.1371/journal.pone.0080705.

Baptista, Marco A. S., Kalpana Merchant, Ted Barrett, Sakshi Bhargava, Dianne K. Bryce, J. Michael Ellis, Anthony A. Estrada, et al. 2020. «LRRK2 Inhibitors Induce Reversible Changes in Nonhuman Primate Lungs without Measurable Pulmonary Deficits». *Science Translational Medicine* 12 (540). https://doi.org/10.1126/scitranslmed.aav0820.

Belluzzi, Elisa, Adriano Gonnelli, Maria-Daniela Cirnaru, Antonella Marte, Nicoletta Plotegher, Isabella Russo, Laura Civiero, et al. 2016. «LRRK2 Phosphorylates Pre-Synaptic N-Ethylmaleimide Sensitive Fusion (NSF) Protein Enhancing Its ATPase Activity and SNARE Complex Disassembling Rate». *Molecular Neurodegeneration* 11 (1): 1. https://doi.org/10.1186/s13024-015-0066-z.

Berwick, Daniel C., George R. Heaton, Sonia Azeggagh, e Kirsten Harvey. 2019. «LRRK2 Biology from Structure to Dysfunction: Research Progresses, but the Themes Remain the Same». *Molecular Neurodegeneration* 14 (1): 49. https://doi.org/10.1186/s13024-019-0344-2.

Bibow, Stefan, Valéry Ozenne, Jacek Biernat, Martin Blackledge, Eckhard Mandelkow, e Markus Zweckstetter. 2011. «Structural Impact of Proline-Directed Pseudophosphorylation at AT8, AT100, and PHF1 Epitopes on 441-Residue Tau». *Journal of the American Chemical Society* 133 (40): 15842–45. https://doi.org/10.1021/ja205836j.

Bjørkøy, Geir, Trond Lamark, Andreas Brech, Heidi Outzen, Maria Perander, Aud Overvatn, Harald Stenmark, e Terje Johansen. 2005. «P62/SQSTM1 Forms Protein Aggregates Degraded by Autophagy and Has a Protective Effect on Huntingtin-Induced Cell Death». *The Journal of Cell Biology* 171 (4): 603–14. https://doi.org/10.1083/jcb.200507002.

Bonnycastle, Katherine, Elizabeth C. Davenport, e Michael A. Cousin. 2020. «Presynaptic Dysfunction in Neurodevelopmental Disorders: Insights from the Synaptic Vesicle Life Cycle». *Journal of Neurochemistry*, maggio. https://doi.org/10.1111/jnc.15035.

Bravo-San Pedro, José M., Mireia Niso-Santano, Rubén Gómez-Sánchez, Elisa Pizarro-Estrella, Ana Aiastui-Pujana, Ana Gorostidi, Vicente Climent, et al. 2013. «The LRRK2 G2019S Mutant Exacerbates Basal Autophagy through Activation of the MEK/ERK Pathway». *Cellular and Molecular Life Sciences: CMLS* 70 (1): 121–36. https://doi.org/10.1007/s00018-012-1061-y.

Chernova, T., J. R. Steinert, C. J. Guerin, P. Nicotera, I. D. Forsythe, e A. G. Smith. 2007. «Neurite Degeneration Induced by Heme Deficiency Mediated via Inhibition of NMDA Receptor-Dependent Extracellular Signal-Regulated Kinase 1/2 Activation». *Journal of Neuroscience* 27 (32): 8475–85. https://doi.org/10.1523/JNEUROSCI.0792-07.2007.

Cogo, Susanna, Claudia Manzoni, Patrick A. Lewis, e Elisa Greggio. 2020. «Leucine-Rich Repeat Kinase 2 and Lysosomal Dyshomeostasis in Parkinson Disease». *Journal of Neurochemistry* 152 (3): 273–83. https://doi.org/10.1111/jnc.14908.

Collins, J., C. Robinson, H. Danhof, C. W. Knetsch, H. C. van Leeuwen, T. D. Lawley, J. M. Auchtung, e R. A. Britton. 2018. «Dietary Trehalose Enhances Virulence of Epidemic Clostridium Difficile». *Nature* 553 (7688): 291–94. https://doi.org/10.1038/nature25178.

Cresto, Noémie, Camille Gardier, Francesco Gubinelli, Marie-Claude Gaillard, Géraldine Liot, Andrew B. West, e Emmanuel Brouillet. 2019. «The Unlikely Partnership between LRRK2 and α-Synuclein in Parkinson's Disease». *The European Journal of Neuroscience* 49 (3): 339–63. https://doi.org/10.1111/ejn.14182.

Dächsel, Justus C, Owen A Ross, Ignacio F Mata, Jennifer Kachergus, Mathias Toft, Ashley Cannon, Matt Baker, et al. 2007. «Lrrk2 G2019S substitution in frontotemporal lobar degeneration with ubiquitin-immunoreactive neuronal inclusions». *Acta neuropathologica* 113 (5): 601–6. https://doi.org/10.1007/s00401-006-0178-1.

DeBosch, Brian J., Monique R. Heitmeier, Allyson L. Mayer, Cassandra B. Higgins, Jan R. Crowley, Thomas E. Kraft, Maggie Chi, et al. 2016. «Trehalose Inhibits Solute Carrier 2A (SLC2A) Proteins to Induce Autophagy and Prevent Hepatic Steatosis». *Science Signaling* 9 (416): ra21. https://doi.org/10.1126/scisignal.aac5472.

Del Roso, Alessandra, Simona Vittorini, Gabriella Cavallini, Alessio Donati, Zina Gori, Matilde Masini, Maria Pollera, e Ettore Bergamini. 2003. «Ageing-Related Changes in the in Vivo

Function of Rat Liver Macroautophagy and Proteolysis». *Experimental Gerontology* 38 (5): 519–27.

Di Maio, Roberto, Eric K. Hoffman, Emily M. Rocha, Matthew T. Keeney, Laurie H. Sanders, Briana R. De Miranda, Alevtina Zharikov, et al. 2018. «LRRK2 Activation in Idiopathic Parkinson's Disease». *Science Translational Medicine* 10 (451). https://doi.org/10.1126/scitranslmed.aar5429.

Ding, Xiao, e Feng Ren. 2020. «Leucine-Rich Repeat Kinase 2 Inhibitors: A Patent Review (2014-Present)». *Expert Opinion on Therapeutic Patents* 30 (4): 275–86. https://doi.org/10.1080/13543776.2020.1729354.

Ferree, Andrew, Maria Guillily, Hu Li, Katelyn Smith, Aki Takashima, Rachel Squillace, Manfred Weigele, James J. Collins, e Benjamin Wolozin. 2012. «Regulation of Physiologic Actions of LRRK2: Focus on Autophagy». *Neuro-Degenerative Diseases* 10 (1–4): 238–41. https://doi.org/10.1159/000332599.

Ferri, Anna L. M., Maurizio Cavallaro, Daniela Braida, Antonello Di Cristofano, Annalisa Canta, Annamaria Vezzani, Sergio Ottolenghi, et al. 2004. «Sox2 Deficiency Causes Neurodegeneration and Impaired Neurogenesis in the Adult Mouse Brain». *Development (Cambridge, England)* 131 (15): 3805–19. https://doi.org/10.1242/dev.01204.

Fiske, Michael, Stephanie Valtierra, Keith Solvang, Michael Zorniak, Michael White, Sara Herrera, Alina Konnikova, Rebecca Brezinsky, e Shubhik Debburman. 2011. «Contribution of Alanine-76 and Serine Phosphorylation in α-Synuclein Membrane Association and Aggregation in Yeasts». *Parkinson's Disease* 2011: 392180. https://doi.org/10.4061/2011/392180.

Fuji, Reina N., Michael Flagella, Miriam Baca, Marco A. S Baptista, Jens Brodbeck, Bryan K. Chan, Brian K. Fiske, et al. 2015. «Effect of Selective LRRK2 Kinase Inhibition on Nonhuman Primate Lung». *Science Translational Medicine* 7 (273): 273ra15. https://doi.org/10.1126/scitranslmed.aaa3634.

Fujikake, Nobuhiro, Minkyoung Shin, e Shigeomi Shimizu. 2018. «Association Between Autophagy and Neurodegenerative Diseases». *Frontiers in Neuroscience* 12: 255. https://doi.org/10.3389/fnins.2018.00255.

Garini, Yuval, Bart J. Vermolen, e Ian T. Young. 2005. «From Micro to Nano: Recent Advances in High-Resolution Microscopy». *Current Opinion in Biotechnology* 16 (1): 3–12. https://doi.org/10.1016/j.copbio.2005.01.003.

Gloeckner, C. J., N. Kinkl, A. Schumacher, R. J. Braun, E. O'Neill, T. Meitinger, W. Kolch, H. Prokisch, e M. Ueffing. 2006. «The Parkinson disease causing LRRK2 mutation I2020T is associated with increased kinase activity». *Hum Mol Genet* 15: 223–32.

Gómez-Suaga, Patricia, Berta Luzón-Toro, Dev Churamani, Ling Zhang, Duncan Bloor-Young, Sandip Patel, Philip G. Woodman, Grant C. Churchill, e Sabine Hilfiker. 2012. «Leucine-Rich Repeat Kinase 2 Regulates Autophagy through a Calcium-Dependent Pathway Involving NAADP». *Human Molecular Genetics* 21 (3): 511–25. https://doi.org/10.1093/hmg/ddr481.

Gonçalves, Susana, e Tiago Fleming Outeiro. 2013. «Assessing the Subcellular Dynamics of Alpha-Synuclein Using Photoactivation Microscopy». *Molecular Neurobiology* 47 (3): 1081–92. https://doi.org/10.1007/s12035-013-8406-x.

Graham, Steven H., e Hao Liu. 2017. «Life and Death in the Trash Heap: The Ubiquitin Proteasome Pathway and UCHL1 in Brain Aging, Neurodegenerative Disease and Cerebral Ischemia». *Ageing Research Reviews* 34 (marzo): 30–38. https://doi.org/10.1016/j.arr.2016.09.011.

Guerreiro, Patrícia Silva, Ellen Gerhardt, Tomás Lopes da Fonseca, Mathias Bähr, Tiago Fleming Outeiro, e Katrin Eckermann. 2016. «LRRK2 Promotes Tau Accumulation, Aggregation and Release». *Molecular Neurobiology* 53 (5): 3124–35. https://doi.org/10.1007/s12035-015-9209-z.

Halbe, L., e A. Rami. 2019. «Trehalase Localization in the Cerebral Cortex, Hippocampus and Cerebellum of Mouse Brains». *Journal of Advanced Research* 18 (luglio): 71–79. https://doi.org/10.1016/j.jare.2019.01.009.

Hara, Taichi, Kenji Nakamura, Makoto Matsui, Akitsugu Yamamoto, Yohko Nakahara, Rika Suzuki-Migishima, Minesuke Yokoyama, et al. 2006. «Suppression of Basal Autophagy in Neural Cells Causes Neurodegenerative Disease in Mice». *Nature* 441 (7095): 885–89. https://doi.org/10.1038/nature04724.

Herzig, Martin C, Carine Kolly, Elke Persohn, Diethilde Theil, Tatjana Schweizer, Thomas Hafner, Christine Stemmelen, et al. 2011a. «LRRK2 Protein Levels Are Determined by Kinase Function and Are Crucial for Kidney and Lung Homeostasis in Mice». *Human Molecular Genetics* 20 (21): 4209–23. https://doi.org/10.1093/hmg/ddr348.

———. 2011b. «LRRK2 Protein Levels Are Determined by Kinase Function and Are Crucial for Kidney and Lung Homeostasis in Mice». *Human Molecular Genetics* 20 (21): 4209–23. https://doi.org/10.1093/hmg/ddr348.

Hickey, M. A., A. Kosmalska, J. Enayati, R. Cohen, S. Zeitlin, M. S. Levine, e M.-F. Chesselet. 2008. «Extensive Early Motor and Non-Motor Behavioral Deficits Are Followed by Striatal Neuronal Loss in Knock-in Huntington's Disease Mice». *Neuroscience* 157 (1): 280–95. https://doi.org/10.1016/j.neuroscience.2008.08.041.

Higashi, Shinji, Darren J. Moore, Michiko Minegishi, Koji Kasanuki, Hiroshige Fujishiro, Tomohiro Kabuta, Takashi Togo, et al. 2011. «Localization of MAP1-LC3 in Vulnerable Neurons and Lewy Bodies in Brains of Patients with Dementia with Lewy Bodies». *Journal of Neuropathology and Experimental Neurology* 70 (4): 264–80. https://doi.org/10.1097/NEN.0b013e318211c86a.

Inoue, Masafumi, Takashi Konno, Kazuki Tainaka, Eiji Nakata, Hiro-O. Yoshida, e Takashi Morii. 2012. «Positional Effects of Phosphorylation on the Stability and Morphology of Tau-Related Amyloid Fibrils». *Biochemistry* 51 (7): 1396–1406. https://doi.org/10.1021/bi201451z.

Kalia, Lorraine V., Anthony E. Lang, Lili-Naz Hazrati, Shinsuke Fujioka, Zbigniew K. Wszolek, Dennis W. Dickson, Owen A. Ross, et al. 2015. «Clinical Correlations with Lewy Body Pathology in LRRK2-Related Parkinson Disease». *JAMA Neurology* 72 (1): 100–105. https://doi.org/10.1001/jamaneurol.2014.2704.

Kheterpal, I., A. Williams, C. Murphy, B. Bledsoe, e R. Wetzel. 2001. «Structural Features of the Abeta Amyloid Fibril Elucidated by Limited Proteolysis». *Biochemistry* 40 (39): 11757–67.

Komatsu, Masaaki, Satoshi Waguri, Tomoki Chiba, Shigeo Murata, Jun-ichi Iwata, Isei Tanida, Takashi Ueno, et al. 2006. «Loss of Autophagy in the Central Nervous System Causes Neurodegeneration in Mice». *Nature* 441 (7095): 880–84. https://doi.org/10.1038/nature04723.

Kopito, R. R. 2000. «Aggresomes, Inclusion Bodies and Protein Aggregation». *Trends in Cell Biology* 10 (12): 524–30.

Kragh, Christine L., Louise B. Lund, Fabia Febbraro, Hanne D. Hansen, Wei-Ping Gai, Omar El-Agnaf, Christiane Richter-Landsberg, e Poul Henning Jensen. 2009. «Alpha-Synuclein Aggregation and Ser-129 Phosphorylation-Dependent Cell Death in Oligodendroglial Cells». *The Journal of Biological Chemistry* 284 (15): 10211–22. https://doi.org/10.1074/jbc.M809671200.

Lichtenberg, M, A Mansilla, V R Zecchini, A Fleming, e D C Rubinsztein. 2011. «The Parkinson's disease protein LRRK2 impairs proteasome substrate clearance without affecting proteasome catalytic activity». *Cell death & disease* 2: e196. https://doi.org/10.1038/cddis.2011.81.

Lis, Pawel, Sophie Burel, Martin Steger, Matthias Mann, Fiona Brown, Federico Diez, Francesca Tonelli, et al. 2018. «Development of Phospho-Specific Rab Protein Antibodies to Monitor in Vivo Activity of the LRRK2 Parkinson's Disease Kinase». *The Biochemical Journal* 475 (1): 1–22. https://doi.org/10.1042/BCJ20170802.

Liu, C., e B. Hu. 2004. «Alterations of N-Ethylmaleimide-Sensitive Atpase Following Transient Cerebral Ischemia». *Neuroscience* 128 (4): 767–74. https://doi.org/10.1016/j.neuroscience.2004.07.025.

Longo, Francesco, Daniela Mercatelli, Salvatore Novello, Ludovico Arcuri, Alberto Brugnoli, Fabrizio Vincenzi, Isabella Russo, et al. 2017. «Age-Dependent Dopamine Transporter Dysfunction and Serine129 Phospho-α-Synuclein Overload in G2019S LRRK2 Mice». *Acta Neuropathologica Communications* 5 (1): 22. https://doi.org/10.1186/s40478-017-0426-8.

Luong, Tinh N., Holly J. Carlisle, Amber Southwell, e Paul H. Patterson. 2011. «Assessment of Motor Balance and Coordination in Mice Using the Balance Beam». *Journal of Visualized Experiments: JoVE*, n. 49 (marzo). https://doi.org/10.3791/2376.

MacIsaac, Sarah, Thaiany Quevedo Melo, Yuting Zhang, Mattia Volta, Matthew J. Farrer, e Austen J. Milnerwood. 2020. «Neuron-Autonomous Susceptibility to Induced Synuclein Aggregation Is Exacerbated by Endogenous Lrrk2 Mutations and Ameliorated by Lrrk2 Genetic Knock-Out». *Brain Communications* 2 (1): fcz052. https://doi.org/10.1093/braincomms/fcz052.

Malhotra, V., L. Orci, B. S. Glick, M. R. Block, e J. E. Rothman. 1988. «Role of an N-Ethylmaleimide-Sensitive Transport Component in Promoting Fusion of Transport Vesicles with Cisternae of the Golgi Stack». *Cell* 54 (2): 221–27.

Mamais, Adamantios, Meera Raja, Claudia Manzoni, Sybille Dihanich, Andrew Lees, Darren Moore, Patrick A Lewis, e Rina Bandopadhyay. 2013. «Divergent α-Synuclein Solubility and Aggregation Properties in G2019S LRRK2 Parkinson's Disease Brains with Lewy Body Pathology Compared to Idiopathic Cases». *Neurobiology of Disease* 58 (ottobre): 183–90. https://doi.org/10.1016/j.nbd.2013.05.017.

Manzoni, Claudia. 2017. «The LRRK2-Macroautophagy Axis and Its Relevance to Parkinson's Disease». *Biochemical Society Transactions* 45 (1): 155–62. https://doi.org/10.1042/BST20160265.

Manzoni, Claudia, e Patrick A. Lewis. 2017. «LRRK2 and Autophagy». *Advances in Neurobiology* 14: 89–105. https://doi.org/10.1007/978-3-319-49969-7_5.

Manzoni, Claudia, Adamantios Mamais, Sybille Dihanich, Phillip McGoldrick, Michael J Devine, Julia Zerle, Eleanna Kara, et al. 2013. «Pathogenic Parkinson's Disease Mutations across the Functional Domains of LRRK2 Alter the Autophagic/Lysosomal Response to Starvation». *Biochemical and Biophysical Research Communications* 441 (4): 862–66. https://doi.org/10.1016/j.bbrc.2013.10.159.

Marin, I. 2006. «The Parkinson disease gene LRRK2: evolutionary and structural insights». *Mol Biol Evol* 23 (12): 2423–33.

Martinez-Vicente, Marta, Guy Sovak, e Ana Maria Cuervo. 2005. «Protein Degradation and Aging». *Experimental Gerontology* 40 (8–9): 622–33. https://doi.org/10.1016/j.exger.2005.07.005.

Meijering, E, M Jacob, J-C F Sarria, P Steiner, H Hirling, e M Unser. 2004. «Design and validation of a tool for neurite tracing and analysis in fluorescence microscopy images». *Cytometry. Part A: the journal of the International Society for Analytical Cytology* 58 (2): 167–76. https://doi.org/10.1002/cyto.a.20022.

Melrose, H L, J C Dächsel, B Behrouz, S J Lincoln, M Yue, K M Hinkle, C B Kent, et al. 2010. «Impaired dopaminergic neurotransmission and microtubule-associated protein tau alterations in human LRRK2 transgenic mice». *Neurobiology of Disease* 40 (3): 503–17. https://doi.org/10.1016/j.nbd.2010.07.010.

Metskas, Lauren Ann, e Elizabeth Rhoades. 2015. «Folding upon Phosphorylation: Translational Regulation by a Disorder-to-Order Transition». *Trends in Biochemical Sciences* 40 (5): 243–44. https://doi.org/10.1016/j.tibs.2015.02.007.

Mohtashami, M., B. A. Stewart, G. L. Boulianne, e W. S. Trimble. 2001. «Analysis of the Mutant Drosophila N-Ethylmaleimide Sensitive Fusion-1 Protein in Comatose Reveals Molecular Correlates of the Behavioural Paralysis». *Journal of Neurochemistry* 77 (5): 1407–17.

Montalto, M., A. Gallo, V. Ojetti, e A. Gasbarrini. 2013. «Fructose, Trehalose and Sorbitol Malabsorption». *European Review for Medical and Pharmacological Sciences* 17 Suppl 2: 26–29.

Mosmann, T. 1983. «Rapid Colorimetric Assay for Cellular Growth and Survival: Application to Proliferation and Cytotoxicity Assays». *Journal of Immunological Methods* 65 (1–2): 55–63.

Naslavsky, N., R. Stein, A. Yanai, G. Friedlander, e A. Taraboulos. 1997. «Characterization of Detergent-Insoluble Complexes Containing the Cellular Prion Protein and Its Scrapie Isoform». *The Journal of Biological Chemistry* 272 (10): 6324–31.

Ness, Daniel, Zhao Ren, Shyra Gardai, Douglas Sharpnack, Victor J. Johnson, Richard J. Brennan, Elizabeth F. Brigham, e Andrew J. Olaharski. 2013. «Leucine-Rich Repeat Kinase 2 (LRRK2)-Deficient Rats Exhibit Renal Tubule Injury and Perturbations in Metabolic and Immunological Homeostasis». *PloS One* 8 (6): e66164. https://doi.org/10.1371/journal.pone.0066164.

Novello, Salvatore, Ludovico Arcuri, Sandra Dovero, Nathalie Dutheil, Derya R. Shimshek, Erwan Bezard, e Michele Morari. 2018. «G2019S LRRK2 Mutation Facilitates α-Synuclein Neuropathology in Aged Mice». *Neurobiology of Disease* 120 (dicembre): 21–33. https://doi.org/10.1016/j.nbd.2018.08.018.

Obeso, J. A., M. Stamelou, C. G. Goetz, W. Poewe, A. E. Lang, D. Weintraub, D. Burn, et al. 2017. «Past, Present, and Future of Parkinson's Disease: A Special Essay on the 200th Anniversary of the Shaking Palsy». *Movement Disorders: Official Journal of the Movement Disorder Society* 32 (9): 1264–1310. https://doi.org/10.1002/mds.27115.

Olanow, C Warren, Daniel P Perl, George N DeMartino, e Kevin St P McNaught. 2004. «Lewy-Body Formation Is an Aggresome-Related Process: A Hypothesis». *The Lancet Neurology* 3 (8): 496–503. https://doi.org/10.1016/S1474-4422(04)00827-0.

Ottaviani, Daniele, Oriano Marin, Giorgio Arrigoni, Cinzia Franchin, Jordi Vilardell, Michele Sandre, Wenwen Li, et al. 2017. «Protein Kinase CK2 Modulates HSJ1 Function through Phosphorylation of the UIM2 Domain». *Human Molecular Genetics* 26 (3): 611–23. https://doi.org/10.1093/hmg/ddw420.

Paisan-Ruiz, C., P. Nath, N. Washecka, J.R. Gibbs, e A.B. Singleton. 2008. «Comprehensive analysis of LRRK2 in publicly available Parkinson's disease cases and neurologically normal controls». *Hum Mutat* 29 (4): 485–90.

Pallanck, L, R W Ordway, M Ramaswami, W Y Chi, K S Krishnan, e B Ganetzky. 1995. «Distinct Roles for N-Ethylmaleimide-Sensitive Fusion Protein (NSF) Suggested by the Identification of a Second Drosophila NSF Homolog». *The Journal of Biological Chemistry* 270 (32): 18742–44.

Pan, Dao, Anthony Sciascia, Charles V. Vorhees, e Michael T. Williams. 2008. «Progression of Multiple Behavioral Deficits with Various Ages of Onset in a Murine Model of Hurler Syndrome». *Brain Research* 1188 (gennaio): 241–53. https://doi.org/10.1016/j.brainres.2007.10.036.

Perez Carrion, Maria, Francesca Pischedda, Alice Biosa, Isabella Russo, Letizia Straniero, Laura Civiero, Marianna Guida, et al. 2018. «The LRRK2 Variant E193K Prevents Mitochondrial Fission Upon MPP+ Treatment by Altering LRRK2 Binding to DRP1». *Frontiers in Molecular Neuroscience* 11: 64. https://doi.org/10.3389/fnmol.2018.00064.

Piccoli, Giovanni, Steven B Condliffe, Matthias Bauer, Florian Giesert, Karsten Boldt, Silvia De Astis, Andrea Meixner, et al. 2011. «LRRK2 controls synaptic vesicle storage and mobilization within the recycling pool». *The Journal of neuroscience: the official journal of the Society for Neuroscience* 31 (6): 2225–37. https://doi.org/10.1523/JNEUROSCI.3730-10.2011.

Piccoli, Giovanni, Franco Onofri, Maria Daniela Cirnaru, Christoph J O Kaiser, Pravinkumar Jagtap, Andreas Kastenmüller, Francesca Pischedda, et al. 2014. «LRRK2 Binds to Neuronal Vesicles through Protein Interactions Mediated by Its C-Terminal WD40 Domain». *Molecular and Cellular Biology*, marzo. https://doi.org/10.1128/MCB.00914-13.

Pischedda, Francesca, Caterina Montani, Julia Obergasteiger, Giulia Frapporti, Corrado Corti, Marcelo Rosato Siri, Mattia Volta, e Giovanni Piccoli. 2018. «Cryopreservation of Primary Mouse Neurons: The Benefit of Neurostore Cryoprotective Medium». *Frontiers in Cellular Neuroscience* 12: 81. https://doi.org/10.3389/fncel.2018.00081.

Pischedda, Francesca, e Giovanni Piccoli. 2015. «The IgLON Family Member Negr1 Promotes Neuronal Arborization Acting as Soluble Factor via FGFR2». *Frontiers in Molecular Neuroscience* 8: 89. https://doi.org/10.3389/fnmol.2015.00089.

Pischedda, Francesca, Joanna Szczurkowska, Maria Daniela Cirnaru, Florian Giesert, Elena Vezzoli, Marius Ueffing, Carlo Sala, et al. 2014. «A Cell Surface Biotinylation Assay to Reveal Membrane-Associated Neuronal Cues: Negr1 Regulates Dendritic Arborization». *Molecular & Cellular Proteomics: MCP* 13 (3): 733–48. https://doi.org/10.1074/mcp.M113.031716.

Plowey, Edward D., Salvatore J. Cherra, Yong-Jian Liu, e Charleen T. Chu. 2008. «Role of Autophagy in G2019S-LRRK2-Associated Neurite Shortening in Differentiated SH-SY5Y Cells». *Journal of Neurochemistry* 105 (3): 1048–56. https://doi.org/10.1111/j.1471-4159.2008.05217.x.

Pountney, Dean L., Mark J. Raftery, Fariba Chegini, Peter C. Blumbergs, e Wei Ping Gai. 2008. «NSF, Unc-18-1, dynamin-1 and HSP90 are inclusion body components in neuronal intranuclear inclusion disease identified by anti-SUMO-1-immunocapture». *Acta Neuropathologica* 116 (6): 603–14. https://doi.org/10.1007/s00401-008-0437-4.

Ramonet, David, João Paulo L Daher, Brian M Lin, Klodjan Stafa, Jaekwang Kim, Rebecca Banerjee, Marie Westerlund, et al. 2011. «Dopaminergic Neuronal Loss, Reduced Neurite Complexity and Autophagic Abnormalities in Transgenic Mice Expressing G2019S Mutant LRRK2». *PloS One* 6 (4): e18568. https://doi.org/10.1371/journal.pone.0018568.

Reid, Suzanne J., Mark I. Rees, Willeke M. C. van Roon-Mom, A. Lesley Jones, Marcy E. MacDonald, Greg Sutherland, Matthew J. During, et al. 2003. «Molecular Investigation of TBP Allele Length: A SCA17 Cellular Model and Population Study». *Neurobiology of Disease* 13 (1): 37–45.

Reinhardt, Peter, Michael Glatza, Kathrin Hemmer, Yaroslav Tsytsyura, Cora S. Thiel, Susanne Höing, Sören Moritz, et al. 2013. «Derivation and Expansion Using Only Small Molecules of Human Neural Progenitors for Neurodegenerative Disease Modeling». *PloS One* 8 (3): e59252. https://doi.org/10.1371/journal.pone.0059252.

Rodríguez-Navarro, Jose A, Laura Rodríguez, María J Casarejos, Rosa M Solano, Ana Gómez, Juan Perucho, Ana María Cuervo, Justo García de Yébenes, e María A Mena. 2010. «Trehalose Ameliorates Dopaminergic and Tau Pathology in Parkin Deleted/Tau Overexpressing Mice through Autophagy Activation». *Neurobiology of Disease* 39 (3): 423–38. https://doi.org/10.1016/j.nbd.2010.05.014.

Rothman, J. E. 1994. «Mechanisms of Intracellular Protein Transport». *Nature* 372 (6501): 55–63. https://doi.org/10.1038/372055a0.

Rubinsztein, David C. 2006. «The Roles of Intracellular Protein-Degradation Pathways in Neurodegeneration». *Nature* 443 (7113): 780–86. https://doi.org/10.1038/nature05291.

Sancenon, Vicente, Sue-Ann Lee, Christina Patrick, Janice Griffith, Amy Paulino, Tiago F. Outeiro, Fulvio Reggiori, Eliezer Masliah, e Paul J. Muchowski. 2012. «Suppression of α-Synuclein Toxicity and Vesicle Trafficking Defects by Phosphorylation at S129 in Yeast Depends on Genetic Context». *Human Molecular Genetics* 21 (11): 2432–49. https://doi.org/10.1093/hmg/dds058.

Sánchez-Danés, Adriana, Yvonne Richaud-Patin, Iria Carballo-Carbajal, Senda Jiménez-Delgado, Carles Caig, Sergio Mora, Claudia Di Guglielmo, et al. 2012. «Disease-Specific Phenotypes in Dopamine Neurons from Human IPS-Based Models of Genetic and Sporadic Parkinson's Disease». *EMBO Molecular Medicine* 4 (5): 380–95. https://doi.org/10.1002/emmm.201200215.

Sarkar, Sovan, Janet E Davies, Zebo Huang, Alan Tunnacliffe, e David C Rubinsztein. 2007. «Trehalose, a Novel MTOR-Independent Autophagy Enhancer, Accelerates the Clearance of Mutant Huntingtin and Alpha-Synuclein». *The Journal of Biological Chemistry* 282 (8): 5641–52. https://doi.org/10.1074/jbc.M609532200.

Schaefer, L. H., D. Schuster, e J. Schaffer. 2004. «Structured Illumination Microscopy: Artefact Analysis and Reduction Utilizing a Parameter Optimization Approach». *Journal of Microscopy* 216 (Pt 2): 165–74. https://doi.org/10.1111/j.0022-2720.2004.01411.x.

Schapansky, Jason, Saurabh Khasnavis, Mark P. DeAndrade, Jonathan D. Nardozzi, Samuel R. Falkson, Justin D. Boyd, John B. Sanderson, Tim Bartels, Heather L. Melrose, e Matthew J. LaVoie. 2018. «Familial Knockin Mutation of LRRK2 Causes Lysosomal Dysfunction and Accumulation of Endogenous Insoluble α-Synuclein in Neurons». *Neurobiology of Disease* 111 (marzo): 26–35. https://doi.org/10.1016/j.nbd.2017.12.005.

Seki, Takahiro, Nana Abe-Seki, Takahiro Kikawada, Hideyuki Takahashi, Kazuhiro Yamamoto, Naoko Adachi, Shigeru Tanaka, Izumi Hide, Naoaki Saito, e Norio Sakai. 2010. «Effect of Trehalose on the Properties of Mutant {gamma}PKC, Which Causes Spinocerebellar Ataxia Type 14, in Neuronal Cell Lines and Cultured Purkinje Cells». *The Journal of Biological Chemistry* 285 (43): 33252–64. https://doi.org/10.1074/jbc.M110.146704.

Sloan, Max, Javier Alegre-Abarrategui, Dawid Potgieter, Anna-Kristin Kaufmann, Richard Exley, Thierry Deltheil, Sarah Threlfell, et al. 2016. «LRRK2 BAC Transgenic Rats Develop Progressive, L-DOPA-Responsive Motor Impairment, and Deficits in Dopamine Circuit Function». *Human Molecular Genetics* 25 (5): 951–63. https://doi.org/10.1093/hmg/ddv628.

Sossi, Vesna, Raul de la Fuente-Fernández, Ramachandiran Nandhagopal, Michael Schulzer, Jessamyn McKenzie, Thomas J. Ruth, Jan O. Aasly, Matthew J. Farrer, Zbigniew K. Wszolek, e Jon A. Stoessl. 2010. «Dopamine turnover increases in asymptomatic LRRK2 mutations carriers». *Movement Disorders* 25 (16): 2717–23. https://doi.org/10.1002/mds.23356.

Steger, Martin, Francesca Tonelli, Genta Ito, Paul Davies, Matthias Trost, Melanie Vetter, Stefanie Wachter, et al. 2016. «Phosphoproteomics Reveals That Parkinson's Disease Kinase LRRK2 Regulates a Subset of Rab GTPases». *ELife* 5. https://doi.org/10.7554/eLife.12813.

Tanji, Kunikazu, Fumiaki Mori, Akiyoshi Kakita, Hitoshi Takahashi, e Koichi Wakabayashi. 2011. «Alteration of Autophagosomal Proteins (LC3, GABARAP and GATE-16) in Lewy Body Disease». *Neurobiology of Disease* 43 (3): 690–97. https://doi.org/10.1016/j.nbd.2011.05.022.

Taylor, J.P., I.F. Mata, e M.J. Farrer. 2006. «LRRK2: a common pathway for parkinsonism, pathogenesis and prevention?» *Trends Mol Med* 12 (2): 76–82.

Taylor, Matthew, e Dario R. Alessi. 2020. «Advances in Elucidating the Function of Leucine-Rich Repeat Protein Kinase-2 in Normal Cells and Parkinson's Disease». *Current Opinion in Cell Biology* 63 (febbraio): 102–13. https://doi.org/10.1016/j.ceb.2020.01.001.

Taymans, Jean-Marc, e Mark R Cookson. 2010. «Mechanisms in Dominant Parkinsonism: The Toxic Triangle of LRRK2, Alpha-Synuclein, and Tau». *BioEssays: News and Reviews in Molecular, Cellular and Developmental Biology* 32 (3): 227–35. https://doi.org/10.1002/bies.200900163.

Tenreiro, Sandra, Katrin Eckermann, e Tiago F. Outeiro. 2014. «Protein Phosphorylation in Neurodegeneration: Friend or Foe?» *Frontiers in Molecular Neuroscience* 7: 42. https://doi.org/10.3389/fnmol.2014.00042.

Tong, Youren, Emilie Giaime, Hiroo Yamaguchi, Takaharu Ichimura, Yumin Liu, Huiqing Si, Huaibin Cai, Joseph V Bonventre, e Jie Shen. 2012. «Loss of Leucine-Rich Repeat Kinase 2 Causes Age-Dependent Bi-Phasic Alterations of the Autophagy Pathway». *Molecular Neurodegeneration* 7: 2. https://doi.org/10.1186/1750-1326-7-2.

Tong, Youren, Hiroo Yamaguchi, Emilie Giaime, Scott Boyle, Raphael Kopan, Raymond J. Kelleher, e Jie Shen. 2010a. «Loss of Leucine-Rich Repeat Kinase 2 Causes Impairment of Protein Degradation Pathways, Accumulation of Alpha-Synuclein, and Apoptotic Cell Death

in Aged Mice». *Proceedings of the National Academy of Sciences of the United States of America* 107 (21): 9879–84. https://doi.org/10.1073/pnas.1004676107.
———. 2010b. «Loss of Leucine-Rich Repeat Kinase 2 Causes Impairment of Protein Degradation Pathways, Accumulation of Alpha-Synuclein, and Apoptotic Cell Death in Aged Mice». *Proceedings of the National Academy of Sciences of the United States of America* 107 (21): 9879–84. https://doi.org/10.1073/pnas.1004676107.
Varshavsky, Alexander. 2017. «The Ubiquitin System, Autophagy, and Regulated Protein Degradation». *Annual Review of Biochemistry* 86 (giugno): 123–28. https://doi.org/10.1146/annurev-biochem-061516-044859.
Verhoef, Lisette G. G. C., Kristina Lindsten, Maria G. Masucci, e Nico P. Dantuma. 2002. «Aggregate Formation Inhibits Proteasomal Degradation of Polyglutamine Proteins». *Human Molecular Genetics* 11 (22): 2689–2700.
Wauters, Fieke, Tom Cornelissen, Dorien Imberechts, Shaun Martin, Brianada Koentjoro, Carolyn Sue, Peter Vangheluwe, e Wim Vandenberghe. 2019. «LRRK2 Mutations Impair Depolarization-Induced Mitophagy through Inhibition of Mitochondrial Accumulation of RAB10». *Autophagy*, aprile. https://doi.org/10.1080/15548627.2019.1603548.
West, A.B., D.J. Moore, C. Choi, S.A. Andrabi, X. Li, D. Dikeman, S. Biskup, et al. 2007. «Parkinson's disease-associated mutations in LRRK2 link enhanced GTP-binding and kinase activities to neuronal toxicity». *Hum Mol Genet* 16 (2): 223–32.
Whaley, N.R., R.J. Uitti, D.W. Dickson, M.J. Farrer, e Z.K. Wszolek. 2006. «Clinical and pathologic features of families with LRRK2-associated Parkinson's disease». *J Neural Transm Suppl*, n. 70: 221–29.
Whiteheart, S. W., T. Schraw, e E. A. Matveeva. 2001. «N-Ethylmaleimide Sensitive Factor (NSF) Structure and Function». *International Review of Cytology* 207: 71–112.
Wiznerowicz, Maciej, e Didier Trono. 2003. «Conditional suppression of cellular genes: lentivirus vector-mediated drug-inducible RNA interference». *Journal of virology* 77 (16): 8957–61.
Wu, Bo, Qi Liu, Chunli Duan, Yaohua Li, Shun Yu, Piu Chan, Kenji Uéda, e Hui Yang. 2011. «Phosphorylation of α-Synuclein Upregulates Tyrosine Hydroxylase Activity in MN9D Cells». *Acta Histochemica* 113 (1): 32–35. https://doi.org/10.1016/j.acthis.2009.07.007.
Xia, Qiangwei, Lujian Liao, Dongmei Cheng, Duc M Duong, Marla Gearing, James J Lah, Allan I Levey, e Junmin Peng. 2008. «Proteomic identification of novel proteins associated with Lewy bodies». *Frontiers in bioscience: a journal and virtual library* 13: 3850–56.
Yakhine-Diop, Sokhna M. S., José M. Bravo-San Pedro, Rubén Gómez-Sánchez, Elisa Pizarro-Estrella, Mario Rodríguez-Arribas, Vicente Climent, Ana Aiastui, Adolfo López de Munain, José M. Fuentes, e Rosa A. González-Polo. 2014. «G2019S LRRK2 Mutant Fibroblasts from Parkinson's Disease Patients Show Increased Sensitivity to Neurotoxin 1-Methyl-4-Phenylpyridinium Dependent of Autophagy». *Toxicology* 324C (luglio): 1–9. https://doi.org/10.1016/j.tox.2014.07.001.
Zaltzman, Roy, Zohar Elyoseph, Nirit Lev, e Carlos R. Gordon. 2020. «Trehalose in Machado-Joseph Disease: Safety, Tolerability, and Efficacy». *Cerebellum (London, England)*, giugno. https://doi.org/10.1007/s12311-020-01150-6.

Table 1

cases	n° syn +ve LBs	n° NSF +ve LBs	% of LBs +ve for NSF
iPD 1	16	6	37
iPD2	22	8	36
iPD3	10	4	40
iPD4	18	4	22
G2019S1	15	5	33
G2019S2	12	3	25

The table lists the number of α-synuclein positive structure (a-syn +), the number of α-synuclein and NSF positive structure (NSF +) and the relative percentage (%) in specimens prepared from substantia nigra region of 4 idiopathic (iPD) and 2 G2019S patients

Figure legends

Figure 1. hG2019S mice show age-dependent motor and cognitive impairment. Wild-type and hG2019S mice were profiled for motor and cognitive abilities at 3, 6, 12 and 18 month. 6 and 12 months-old hG2019S mice are characterized by an impaired motor coordination and cognitive performance. In detail, we measured spontaneous motor activity in terms of number of horizontal (A) and vertical counts in 3 hours, time to cross a 6-mm width beam (C), time to reach the ground from a supra-elevated platform (D), time spent on rotarod running at 12 rpm (E) or 32 rpm (F), total resistance on 12 rpm running rotarod (G), and ability to recognize novel object compared to the familiar one (H). Data are shown as mean ±SEM; n=7-18. * $p<0.05$, ** $p<0.01$, *** $p<0.001$,****$p<0.0001$ versus aged-matched wild-type.

Figure 2. NSF aggregation in hG2019S mice. NSF accumulates in perinuclear aggregates decorated by LC-3 (A) and p62 (B) in DIV14 cortical neurons prepared from hG2019S mice. Images are shown in pseudo color (NSG green, LC-3 and p62 red, DAPI blue). Scale bar= 10μm. DIV14 cortical cultures from wild-type or hG2019S mice were assayed by filter retardation assay to isolate high-molecular weight form of NSF (HMW) or by dot-blot to measure total NSF protein (C). The graphs report NSF aggregation expressed as HMW fold over total NSF. Data are shown as mean ±SEM, n=8. * $p<0.05$ versus wild-type (D). The biochemical analysis of brain homogenate shows that NSF is resistant to proteinase K degradation in sample prepared from of 6-months old hG2019S mice. Arrowhead indicates the band corresponding to full length NSF (E). The graphs

report the amount of full length NSF protein expressed as optical density after digestion with 0.5 μg/ml proteinase K. Data are shown as mean ±SEM, n=8. * $p<0.05$ versus wild-type (F). NSF accumulates in aggregates in substantia nigra and striatum (G) as well ass in cortex and hippocampus (H) in 6-months hG2019S LRRK2 mice. Scale bar= 10μm.

Figure 3. NSF in human-derived samples. NSF distribution in the Triton-X100 (A) or SDS (B) soluble fraction in PD specimens. Graph reports NSF optical density in the Triton-X100 (C) or SDS (D) soluble fraction, normalized versus actin amount. Data are shown as mean ±SEM, n=4-5. * $p<0.05$ versus control. Post-mortem analysis of nigra specimen shows that NSF decorates α-synuclein positive lewy bodies and lewy neurite in G2019S PD patients. Scale bar= 10μm (E). Induced dopaminergic neurons differentiated from two independent G2019S patients (G2019S 1 and 2) as well as gene-corrected counterpart (GC 1 and 2) were assayed by filter retardation assay to isolate high-molecular weight form of NSF (HMW) or by dot-blot to measure total NSF protein (total) (F). The graphs report NSF aggregation expressed as HMW fold over total NSF. Data are shown as mean ±SEM, n=8. ** $p<0.001$ versus wild-type (G).

Figure 4. LRRK2 phosphorylation induces NSF aggregation. NSF is phosphorylated at Thr645 in G2019S PD-patients brain (A). The graphs report NSF phosphorylation at Thr645 fold over total NSF (B) as well as NSF relative amount (C). Data are shown as mean ±SEM, n=8. * $p<0.05$. NSF is phosphorylated at Thr645 in hG2019S mice brain (D). The graphs report NSF phosphorylation at Thr645 fold over total NSF (E). Data are shown as mean ±SEM, n=8. *, ** $p<0.05$, 0.01 versus wild-type. The combined ribbon, stick and sphere representation showing the overall architecture of NSF hexamer structure from human (PDB ID: 3J94) as well as the positions of T645 and two bound ATP molecules in one NSF monomer. In this drawing, the six NSF monomers are shown in different colors, and the side chain of T645 is shown in the sphere mode and the bound ATP in the stick mode. The missing region between residue 456 and 479 in the NSF monomer is represented by a dashed pink line (F). The enlarged view of a NSF monomer in blue in panel G. Notably, the side chain of T645 is very close to the bound ATP molecule on the D2 domain (G). LRRK2 phosphorylation influences NSF aggregation. We assayed the solubility profile of NSF in sample prepared from DIV14 wild-type or hG2019S cortical neurons and treated with vehicle (DMSO) or the LRRK2 kinase inhibitor GSK2578215A (GSK, 0.2 μM, 18 hours). Short and long exposure of anti-NSF western-blot are reported (H). The graphs report the amount of NSF present in the Triton-X100 insoluble fraction, expressed as fold over total NSF. Data are shown as mean ±SEM, n=11. ** $p<0.01$ versus wild-type DMSO (I). We assayed the solubility profile of FLAG- and HA-NSF in sample prepared from HEK293 cell over-expressing wild-type or phosphomimetic T645D Strep-

FLAG-NSF isoform together with HA-NSF wild-type. Strep-FLAG NSF T465D is present in the Triton-X100 insoluble fraction and sequesters HA-NSF wild-type (J). The graphs report the amount of FLAG-NSF (K) and HA-NSF (L) present in the Triton-X100 insoluble fraction, expressed as fold over total NSF. We transfected in HEK293T cells myc-ubiquitin together with Strep-FLAG-NSF WT or T645D. We purified on streptavidin-beads NSF protein and assessed ubiquitination level by western-blotting with anti-myc antibody. Arrowheads indicate putative NSF low molecular weight fragments detected by anti-FLAG antibody (M). The graphs report NSF ubiquitination in presence of myc-ubiquitin wild-type, calculated as anti-myc optical density normalized versus total NSF yield (N) and NSF fragmentation, expressed as ratio of low molecular weight NSF fragments over high molecular weight NSF optical density (O). Data are shown as mean ±SEM, n=7. ** $p<0.01$ versus wild-type.

Figure 5. LRRK2 phosphorylation triggers NSF toxicity. Representative images of DIV14 Wild-type and hG2019S cortical neurons transduced at DIV4 with mCherry expressing viruses (control) or viruses co-expressing mCherry and wild-type Strep-FLAG NSF WT, phospho-null variant T645A or T645D. Where indicated, cells were chronically treated from DIV4 to DIV14 with DMSO or GSK2578215A (GSK, 0.2 μM, every two day). Cell were then processed for imaging purposes at DIV14, scale bar= 40um (A). The graph reports the number of neurite per neuron. Data are shown as mean ±SEM, n=14. *** $p<0.001$ versus NSF WT in wild-type neuron, °°° $p<0.001$ versus control infection in wild-type neuron, ## $p<0.01$ versus NSF WT in hG2019S neurons DMSO (B). Neuronal cultures were infected and treated as above and then processed for MTT assay at DIV14. Graph reports toxicity, expressed as 100-relative viability (C). Data are shown as mean ±SEM, n=18. ** $p<0.01$ versus NSF WT in wild-type neurons, # $p<0.01$ versus versus NSF WT in wild-type neurons DMSO,°° $p<0.001$ versus control infection in wild-type neuron.

Figure 6. Trehalose treatment rescues histochemical pathological hallmark of hG2019S mice in substantia nigra. Wild-type and hG2019S mice were treated starting at 5 month with trehalose (1% in drinking water) and processed for imaging analysis at 6-month. Nigra sections were stained with anti NSF, anti TH and anti cleaved caspase 3 antibodies and counterstained with hematoxylin to visualize nuclei. hG2019S mice are characterized by NSF aggregation and caspase-3 cleavage in nigra. Trehalose treatment reduces NSF aggregation and cleaved-caspase 3 signal, scale bar = 50 μm (A). The graph reports number of NSF aggregates (B), TH optical density (C) and number of caspase-3 positive cells (D) detected in 0.1 mm^2 area. Data are shown as mean ±S.E, n=6. *** $p<0.001$ versus wild-type, same treatment, $$$ $p<0.001$ versus water, same genotype.

Figure 7. Trehalose treatment rescues histochemical pathological hallmark of hG2019S mice in striatum. Wild-type and hG2019S mice were treated starting at 5 month with trehalose (1% in drinking water) and processed for imaging analysis at 6-month. Striatal sections were stained with anti NSF, anti TH and anti cleaved caspase 3 antibodies and counterstained with hematoxylin to visualize nuclei (A). The graph reports number of NSF aggregates (B), TH optical density (C) and number of caspase-3 positive cells (D) detected in 0.1 mm^2 area. Data are shown as mean ±S.E, n=6. *** $p<0.001$ versus wild-type, same treatment, $$$ $p<0.001$ versus water, same genotype.

Figure 8. Trehalose treatment rescues histochemical pathological hallmark of hG2019S mice in cortex and hippocampus. Wild-type and hG2019S mice were treated starting at 5 month with trehalose (1% in drinking water) and processed for imaging analysis at 6-month. Brain sections encompassing cortical area or hippocampus were stained with anti NSF and anti cleaved caspase 3 antibodies and counterstained with hematoxylin to visualize nuclei. hG2019S mice are characterized by NSF aggregation and caspase-3 cleavage in cortex and hippocampus. Trehalose treatment reduces NSF aggregation and cleaved-caspase 3 signal (A). The graph reports number of NSF aggregates in cortex (B) and hippocampus (C) as well as number of caspase-3 positive cells in in cortex (D) and hippocampus (E) detected in 0.1 mm^2 area. Data are shown as mean ±S.E, n=5. *, *** $p<0.05$, $p<0.001$ versus wild-type, same treatment, $$$ $p<0.001$ versus water, same genotype.

Figure 9. Trehalose treatment rescues motor and cognitive defects of hG2019S mice. Wild-type and hG2019S mice were treated starting at 5 month with trehalose (1% in drinking water) and profiled for motor and cognitive abilities at 6 months. hG2019S mice are characterized by an impaired motor coordination and cognitive performance. In detail, we measured spontaneous motor activity in terms of number of horizontal (A) and vertical (B) counts in 3 hours, time to cross a 12- and 6-mm width beam (C), time to reach the ground from a supra-elevated platform (D), time spent on rotarod running at 12 rpm (E) or 32 rpm (F) over 4 trials (T_1-T_4), total resistance on 12 rpm running rotarod (G), and ability to recognize novel object compared to the familiar one (H). Data are shown as mean ±SEM; n=7-18. * $p<0.05$, ** $p<0.01$, *** $p<0.001$, **** $p<0.0001$ versus wild-type, same treatment, $ $p<0.05$, $$ $p<0.01$, $$$ $p<0.001$ versus water, same genotype.

Supplementary figure 1. hG2019S mice present proteinaceous aggregates. Wild-type and hG2019S mice were processed for imaging analysis at 6-month. Brain sections were stained with anti LC-3 antibodies and counterstained with hematoxylin to visualize nuclei. Scale bars = 50μm. We reported a peculiar LC3-immunoreactivity in the nigra, cortex, and hippocampus specimen

prepared from hG2019S mice brain. Insets highlight differences in LC3 immunoreactivity in neurons (2X higher magnification). We noticed intense LC3 staining surrounding *bona fide* pale bodies (indicated by the asterisk) in nigra (e-f), cortex (q-r) and hippocampus (w-x).

Supplementary figure 2. Wild-type and hG2019S mice were processed for imaging analysis at 6-month. Brain sections were stained with anti synuclein (A) or anti Rab3A (B) antibodies and counterstained with hematoxylin to visualize nuclei. Scale bars= 50µm.

Supplementary figure 3. We performed a biochemical analysis of cortical (C), hippocampal (H), and striatal (S) samples harvested from 6 months old wild-type and hG2019S mice brains (A). The graphs report LRRK2 phosphorylation at Ser935 fold over total LRRK2 (B), relative LRRK2 (C), and NSF (D) amount. Data are shown as mean ±SEM, n=8. The table lists the numer of α-synuclein positive structure (a-syn +) positive for NSF staining (NSF +) and the relative percentage (%) in a 4 iPD and 2 GS patients (E). We performed a western-blot analysis to profile the maturation of G2019S or gene-corrected neural precursor cell to dopaminergic neurons. Anti-nestin antibody stains immature proliferating cells while TH mature DA-neurons. I: expansion media; II: ventral CNS neuron differentiation medium; III maturation medium; IV: differentiation medium (F). Immunofluorescence characterization of terminally differentiated NPC shows the expression of β-III-tubulin, synapsin and TH proteins. Scale bars = 10µm (G).

Supplementary figure 4. Validation of a polyclonal anti P-Thr645-NSF antibody. HEK293 cells were transfected with LRRK2-G2019S and FLAG-tagged wild-type NSF protein. 48h post transfection cells were treated with increasing doses of MLi-2 for 4 hours, then lysed and analyzed (40µg of proteins) by immunoblotting (A). HEK293 cells were transfected with FLAG-tagged wild-type NSF protein or NSF T645A or the phosphomimetics NSF T645E and T645D variant together with GFP or LRRK2-G2019S. Upon solubulization, lysates (40µg of proteins) were subjected to immunoblotting (B). Affinity purified anti- P-Thr645-NSF was used for immunoblot at 1:1000 dilution (in 3% BSA in TBS-T), and in the presence of an excess (5X) of non-phosphorylated peptide antigen (KKAPPQGRKLLIIGTTSRKDVLQEME). LRRK2 phosphorylation influences NSF aggregation. We assayed the solubility profile of NSF in sample prepared from N2A cell over-expressing LRRK2 K1906M or LRRK2 G2019S variants and treated with vehicle (DMSO) or the LRRK2 kinase inhibitor GSK2578215A (GSK, 0.2 mM, 18 hours) (C). The graphs report the

amount of NSF present in the Triton-X100 insoluble fraction, expressed as fold over total NSF. Data are shown as mean ±SEM, n=7. ** $p<0.01$ versus wild-type, same treatment; # $p<0.05$ versus G2019S DMSO (D). NSF aggregates in G2019S LRRK2 cellular models independently from proteasome activity. Wild-type and hG2019S DIV14 cortical neurons were treated with 100nM MG-132 or vehicle (DMSO) for 48 hours and then assayed by filter retardation assay to isolate high molecular weight (HMW) form of NSF or by dot-blot to measure total NSF protein. NSF appears in HMW aggregates in wild-type neurons upon proteasome impairment and in vehicle treated hG2019S neurons (E). The graphs report NSF aggregation expressed as HMW fold over total NSF. Data are shown as mean ±SEM, n=8. *** $p<0.001$ versus wild-type, same treatment, ## $p<0.01$ versus DMSO, same genotype (F). We analysed 20S proteasome activity in brain samples prepared from 6- or 12-months old mice. The graph reports relative fluorescence at 520-530 nm and is expressed as mean ±SEM, n= 4 (G).

Supplementary figure 5. Inorganic phosphate (Pi) generated by ATP hydrolysis in the presence of NSF wild-type and T645D mutant was measured with the Malachite Green Assay at 120min. Data are represented as means ± S.E.; n=3, **=$p<0.01$ Student T-test (A). Kinetic constants were obtained by data fitting with the Michaelis-Menten kinetic model Y = Vmax*S/(Km + [S]). Vmax NSF wild-type=3.6 µmol/min NSF T645D=4 µmol/min; Km NSF wild-type=188 µM Km NSF T645D=180 µM. Extra sum-of-squares F test was used for statistical analysis; n=3 ***$p<0.001$ (B).

HEK293 cell over-expressing Strep-FLAG-NSF wild-type or phosphomimetic T645D isoform and treated with vehicle (DMSO) or MG-132 (10 µM, 18 hours) were analysed by filter retardation assay to isolate high molecular weight (HMW) form of NSF or by dot-blot to measure total NSF protein (C). The graphs report NSF aggregation expressed as ratio of HMW over total NSF optical density. Data are shown as mean ±SEM, n=5. ** $p<0.01$ versus wild-type, same treatment (D). Size exclusion chromatography fractions of HEK293T expressing ectopic Strep-FLAG-NSF wild-type or T645D alone spotted onto nitrocellulose membrane and probed with anti-flag antibody. Theoretical molecular weight are: V0 at fraction 8.5, 669kDa at fraction 12, 449kDa at fraction 13 (E). The graph reports the intensity of each dot (fraction) normalized by the integrated intensities. Column void volume is 7.5 ml, n=3 (F). We transfected in HEK293T cells myc-ubiquitin wild-type, K48R, K63R or K29/48/63 R together with Strep-FLAG-NSF WT or T645D. We purified on streptavidin-beads NSF protein and assessed ubiquitination level by western-blotting with anti-myc antibody. Arrowheads indicate putative NSF low molecular weight fragments detected by anti-FLAG antibody (G). The graphs H, J report NSF ubiquitination calculated as anti-myc optical

density normalized versus total NSF wild-type (H) or T645D (J) yield and expressed as fold over ubiquitin wild-type condition. The graphs I, K and NSF fragmentation, expressed as ratio of low molecular weight NSF fragments over high molecular weight NSF wild-type (I) or T645D (K) optical density and expressed as fold over ubiquitin wild-type condition. Data are shown as mean ±SEM, n=7. *, $p<0.01$, ** $p<0.01$ versus ubiquitin wild-type, one-sample T-test.

Supplementary figure 6. Wild-type and hG2019S cortical neurons were infected at DIV4 with mCherry expressing viruses or viruses co-expressing mCherry and wild-type Strep-FLAG NSF (NSF WT) or Thr645Ala Strep-FLAG NSF (NSF T645A). Cell were chronically treated from DIV4 to DIV14 with DMSO or GSK2578215A (0.2 μM, every two day). Cell were then solubilised and processed for western-blotting to assess ectopic NSF expression, LRRK2 phosphorylation and total LRRK2 level (A). DIV13 Wild-type and hG2019S cortical neurons were treated with vehicle (water) or trehalose (100 mM, 1 day) alone or in combination with NH4Cl (5mM, 2 hours) and then processed for western-blotting to evaluate the induction of autophagy, indicated by the appearance of LC3II band (B). The graph reports LC3II/LC3I ratio. Data are shown as mean ±SEM, n=8. *** $p<0.001$ versus water (C). We assayed by filter retardation assay the presence of NSF in high molecular weight aggregates in sample prepared from HEK293 cell over-expressing NSF wild-type and treated with vehicle (DMSO) or MG-132 (10 μM, 18 hours) alone or in combination with trehalose (100 mM, 18 hours) (HMW) as well as total NSF expression (total) via dot-blot on nitrocellulose membrane (D). The graphs report NSF aggregation expressed as ratio of HMW over total NSF optical density. Data are shown as mean ±SEM, n=8. ** $p<0.01$ versus DMSO; # $p<0.05$ versus control treatment (E). We assessed by filter retardation assay NSF aggregation in brain specimen prepared from 6-month wild-type and hG2019S mice treated with trehalose (1% in drinking water, 1 month). Trehalose treatment reduces HMW NSF forms in cortical specimen obtained from 6 months mice (E). The graphs report NSF aggregation expressed as ratio of HMW over total NSF optical density. Data are shown as mean ±SEM, n=6. * $p<0.05$ versus wild-type, same treatment, ## $p<0.01$ versus water, same genotype (G). Trehalose treatment does not influence mice weight. The graph reports mice weight along the 4 week treatment. Data are shown as mean ±SEM, n=10 (H).

Supplementary figure 7. Wild-type and hG2019S mice were treated starting at 10 month with trehalose (1% in drinking water) and profiled for motor and cognitive abilities at 12 month. In detail, we measured spontaneous motor activity in terms of number of horizontal (A) and vertical (B) counts in 3 hours, time to cross a 6-mm or 12-mm width beam (C), time to reach the ground

from a supra-elevated platform (D), time spent on rotarod running at 12 rpm (E) or 32 rpm (F), over 4 trials (T_1-T_4), total resistance on 12 rpm running rotarod (G) and ability to recognize novel object (H). Data are shown as mean ±SEM; n=7-18. * $p<0.05$, ** $p<0.01$, *** $p<0.001$,**** $p<0.0001$ versus wild-type, same treatment, $ $p<0.05$, $$$ $p<0.001$ versus water, same genotype.

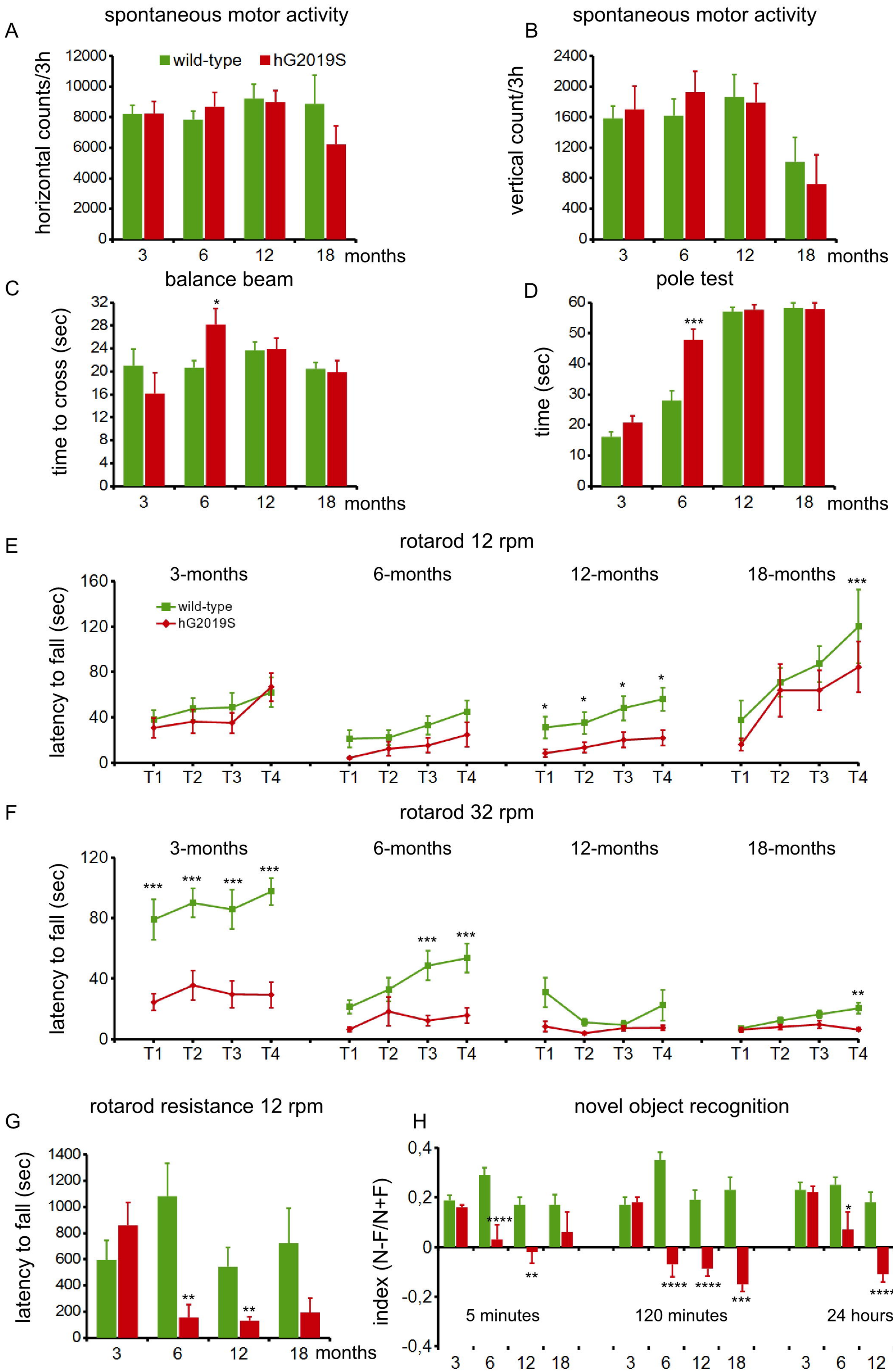
A
spontaneous motor activity
wild-type
hG2019S
horizontal counts/3h
months
B
spontaneous motor activity
vertical count/3h
months
C
balance beam
time to cross (sec)
months
D
pole test
time (sec)
months
E
rotarod 12 rpm
3-months
6-months
12-months
18-months
wild-type
hG2019S
latency to fall (sec)
F
rotarod 32 rpm
3-months
6-months
12-months
18-months
latency to fall (sec)
G
rotarod resistance 12 rpm
latency to fall (sec)
months
H
novel object recognition
index (N-F/N+F)
5 minutes
120 minutes
24 hours

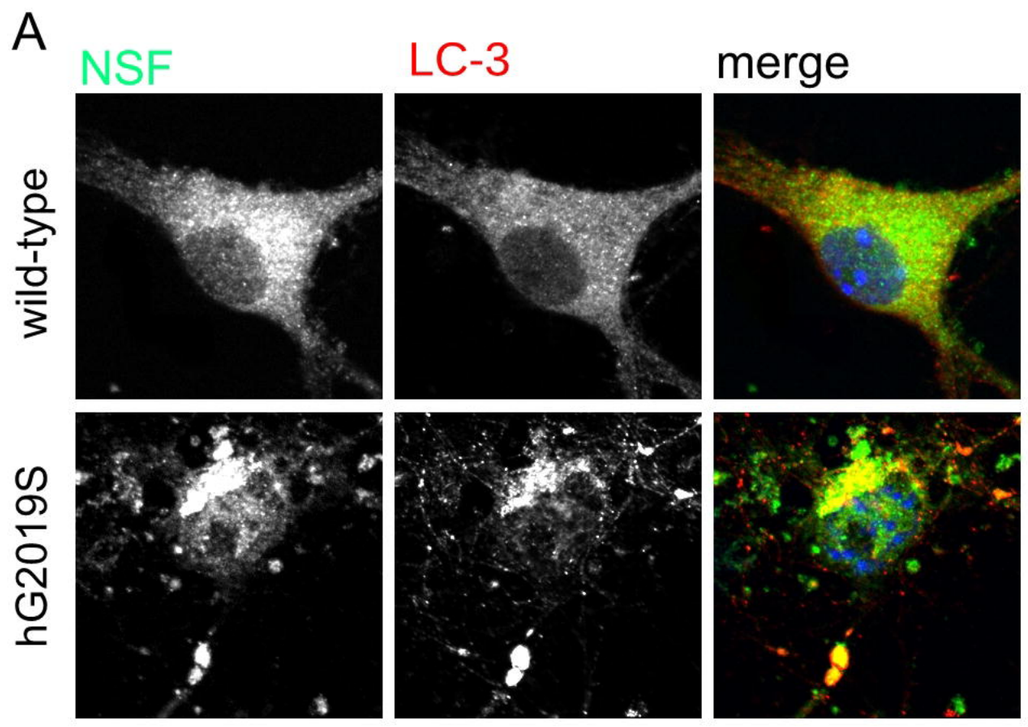
A
NSF
LC-3
merge
wild-type
hG2019S

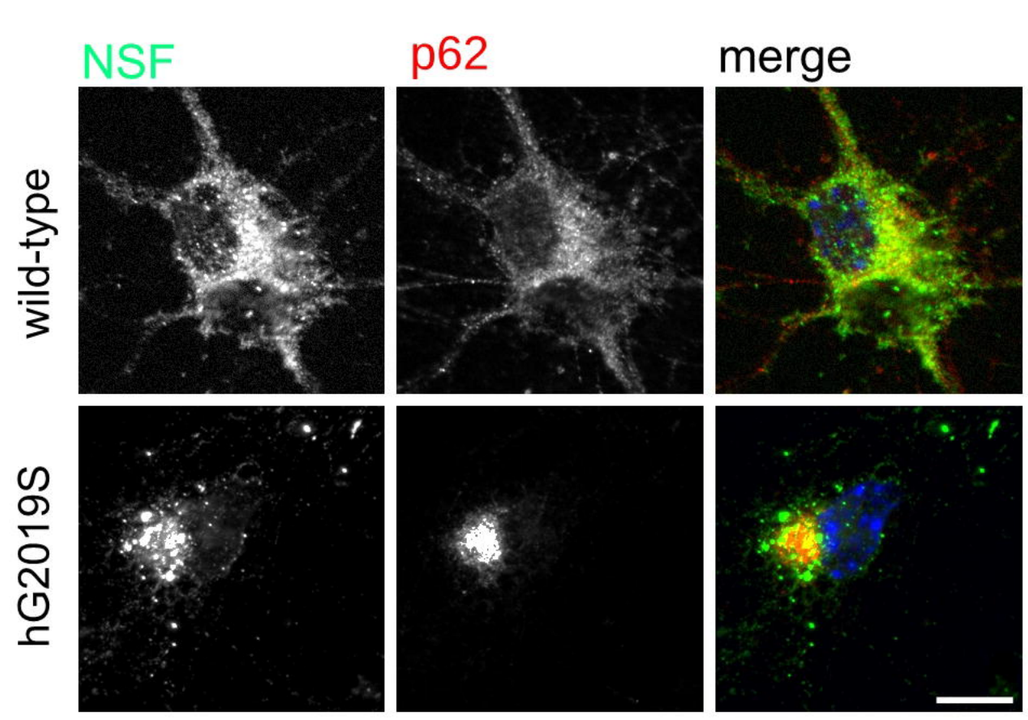
B
NSF
p62
merge
wild-type
hG2019S

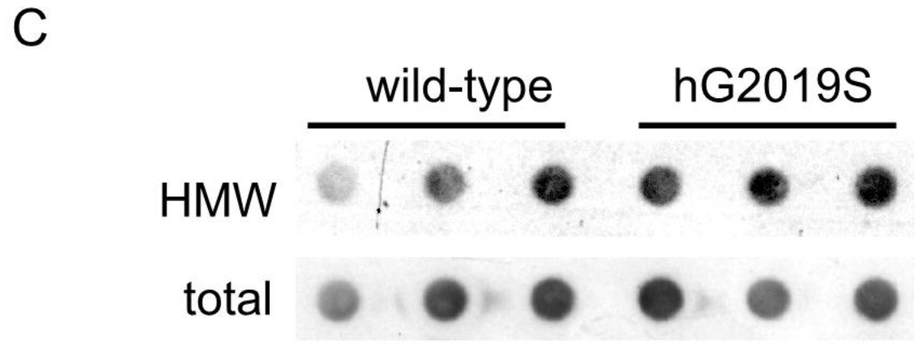
C
wild-type
hG2019S
HMW
total

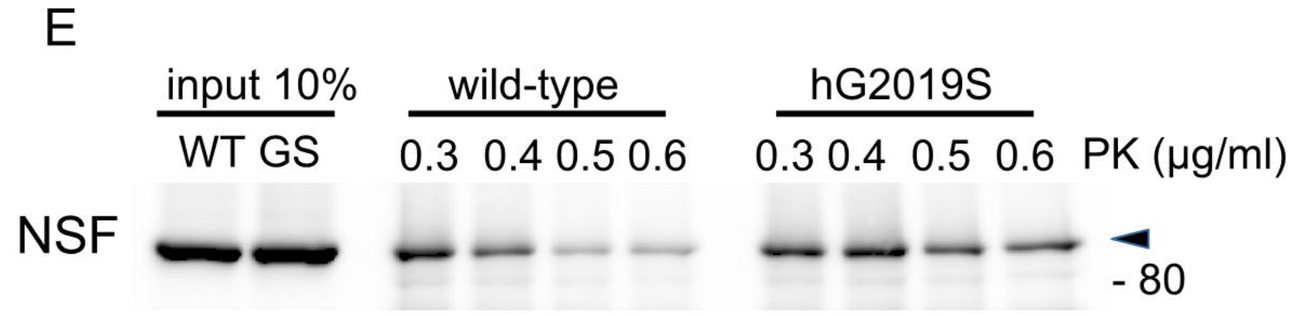
E
input 10%
wild-type
hG2019S
WT GS
0.3 0.4 0.5 0.6
0.3 0.4 0.5 0.6
PK (µg/ml)
NSF
- 80

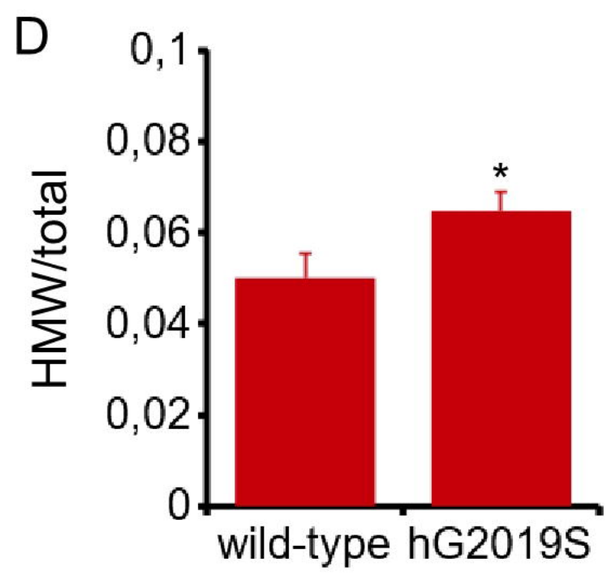
D
HMW/total
0,1
0,08
0,06
0,04
0,02
0
*
wild-type
hG2019S

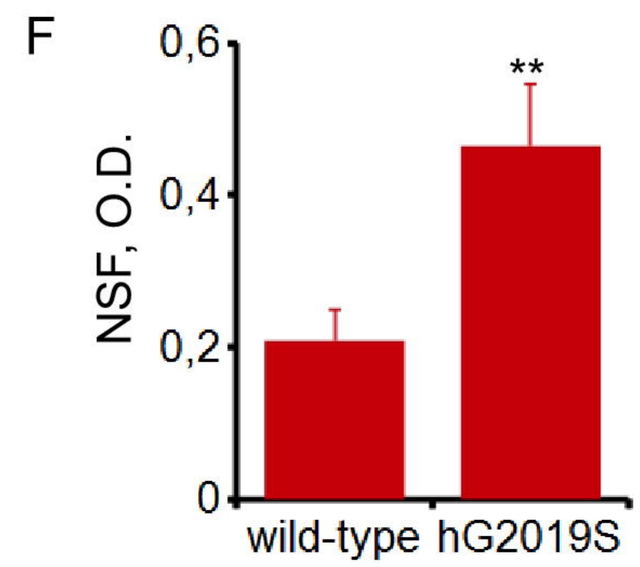
F
NSF, O.D.
0,6
0,4
0,2
0
**
wild-type
hG2019S

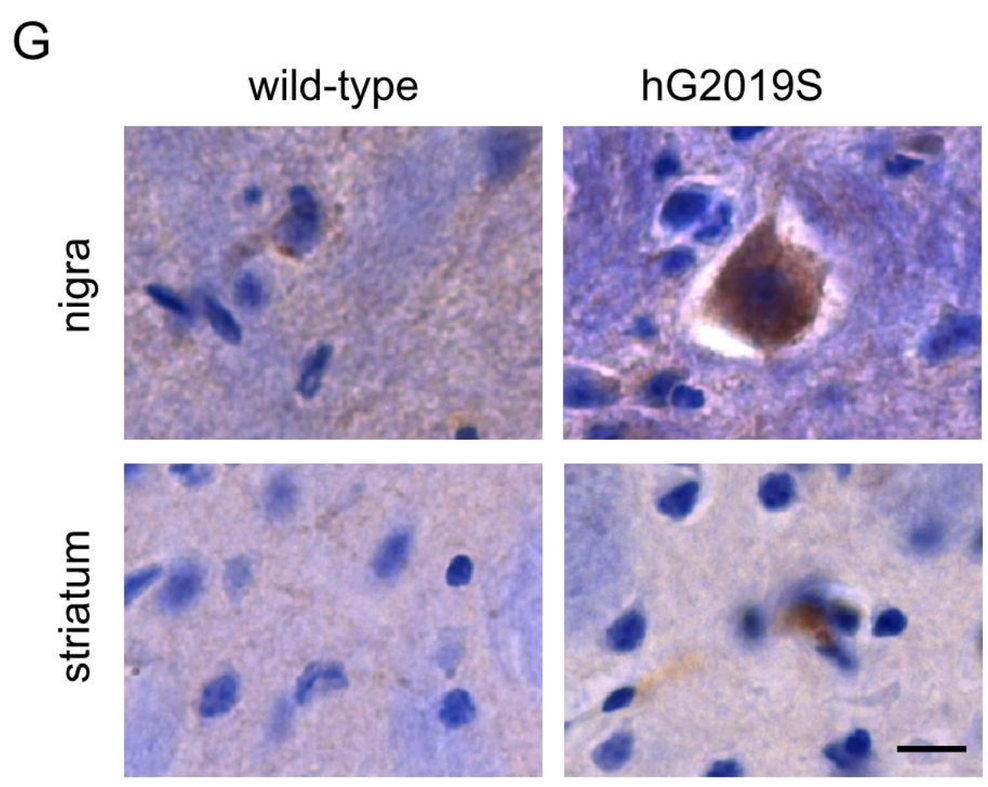
G
wild-type
hG2019S
nigra
striatum

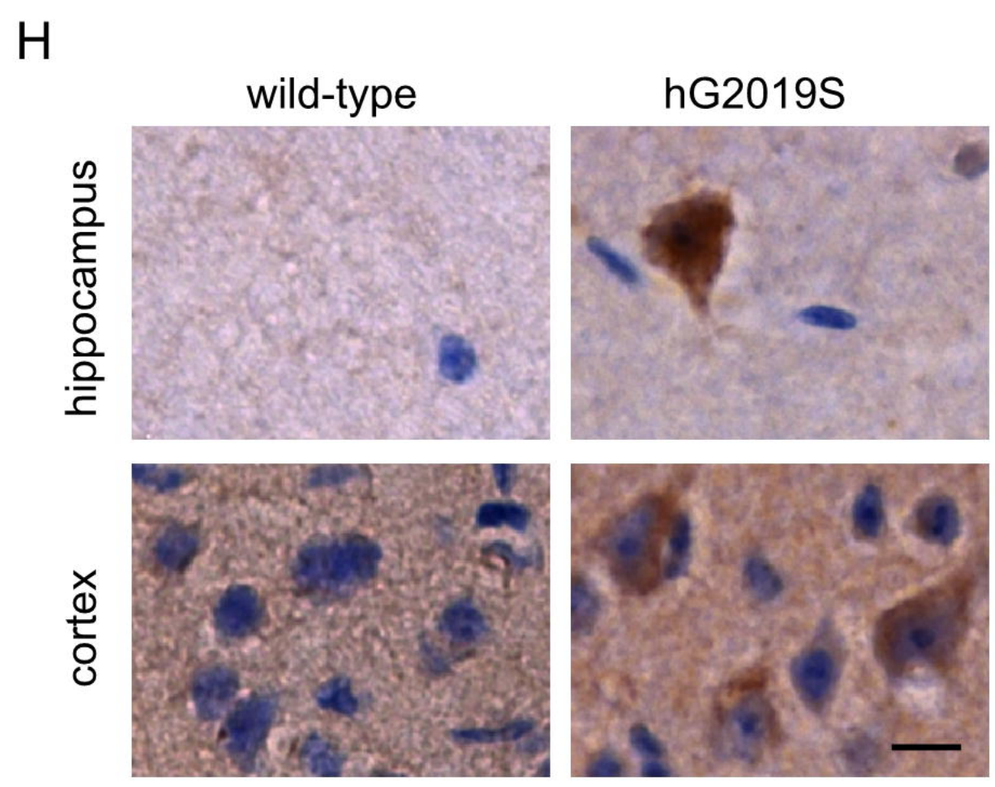
H
wild-type
hG2019S
hippocampus
cortex

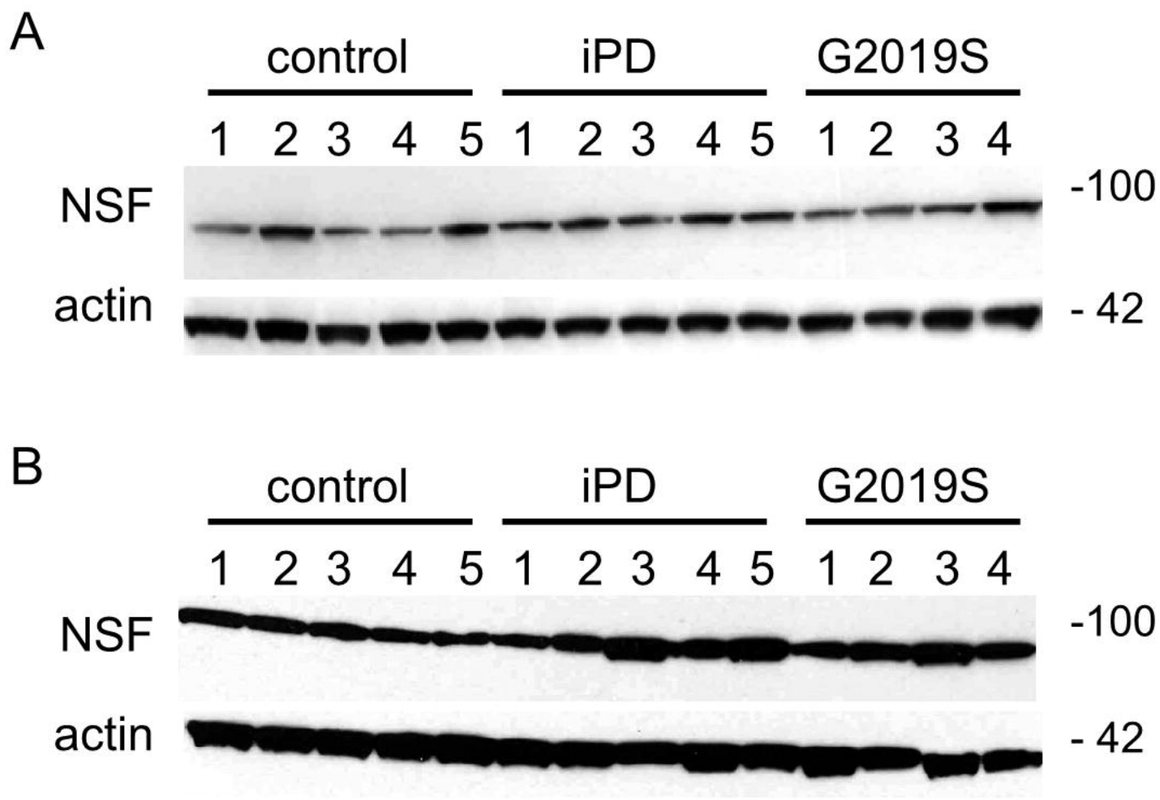
A
control
iPD
G2019S
1 2 3 4 5 1 2 3 4 5 1 2 3 4
NSF
actin
-100
- 42
B
control
iPD
G2019S
1 2 3 4 5 1 2 3 4 5 1 2 3 4
NSF
actin
-100
- 42

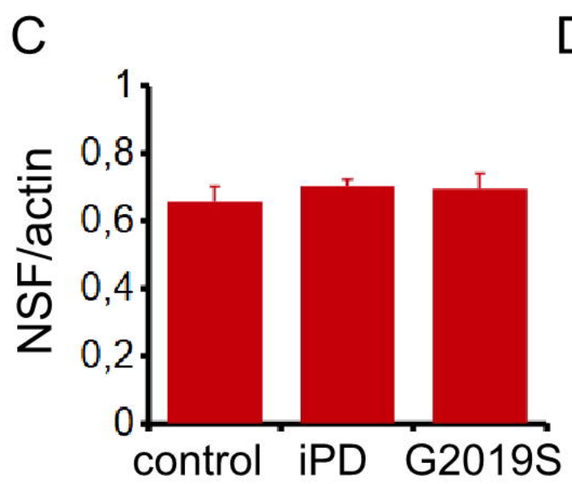
C
NSF/actin
1
0,8
0,6
0,4
0,2
0
control
iPD
G2019S

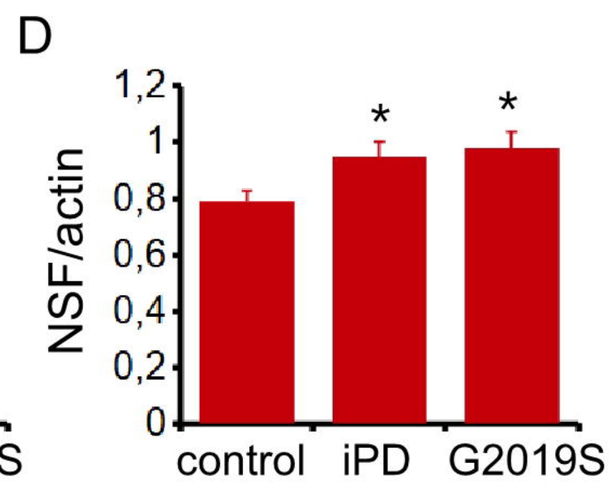
D
NSF/actin
1,2
1
0,8
0,6
0,4
0,2
0
*
*
control
iPD
G2019S

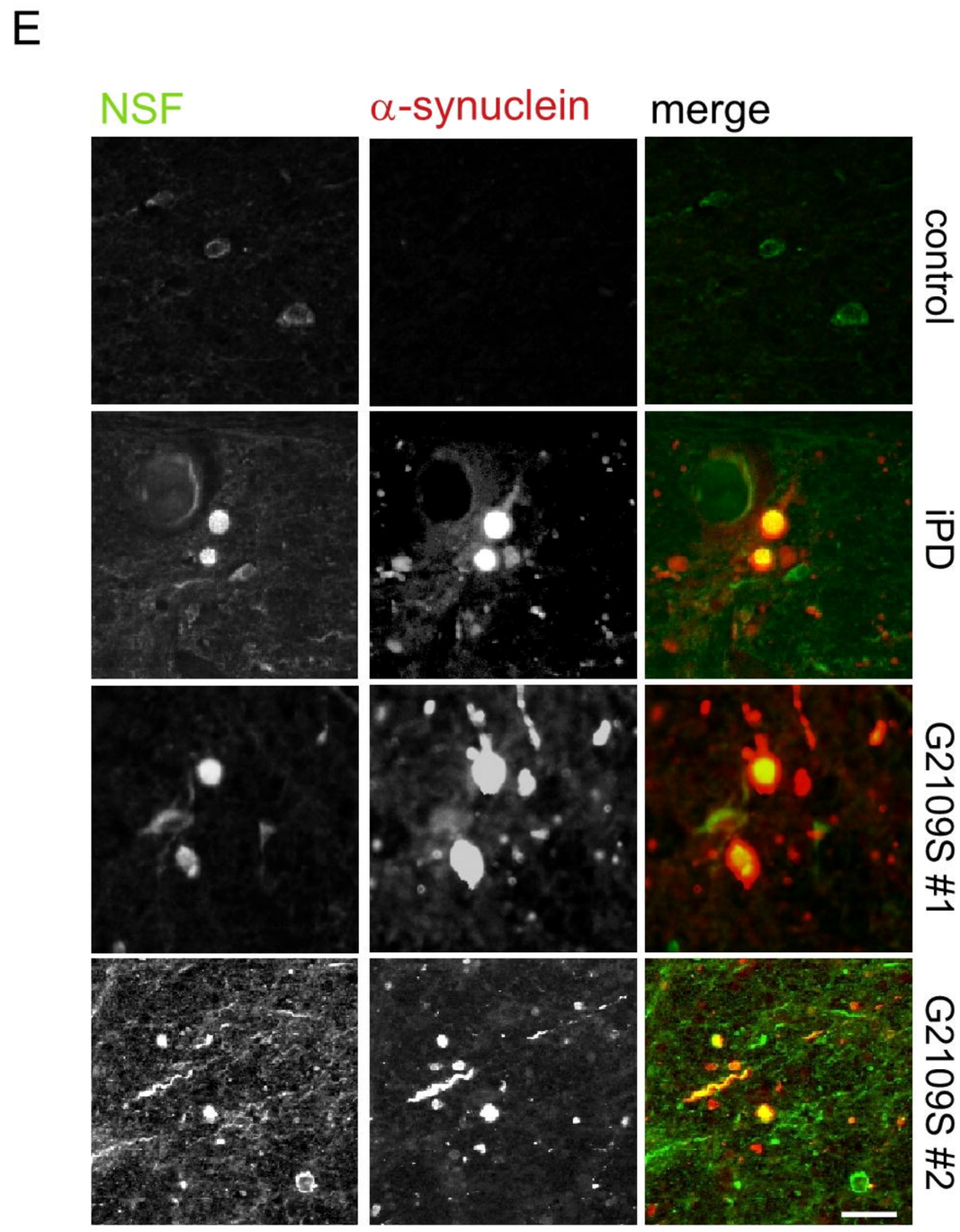
E
NSF
α-synuclein
merge
control
iPD
G2109S #1
G2109S #2

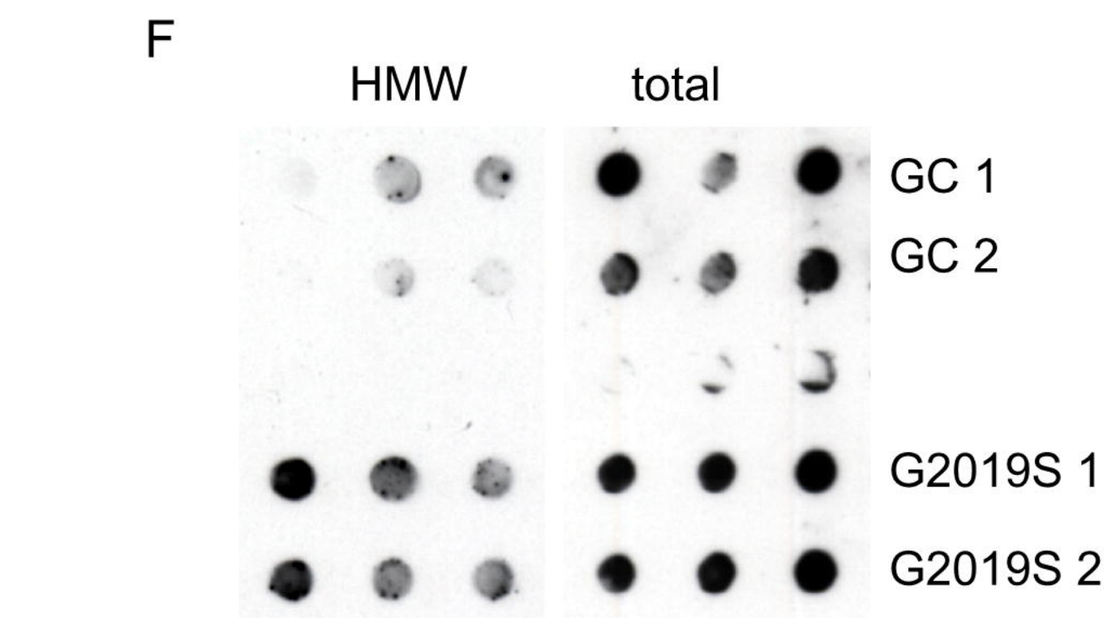
F
HMW
total
GC 1
GC 2
G2019S 1
G2019S 2

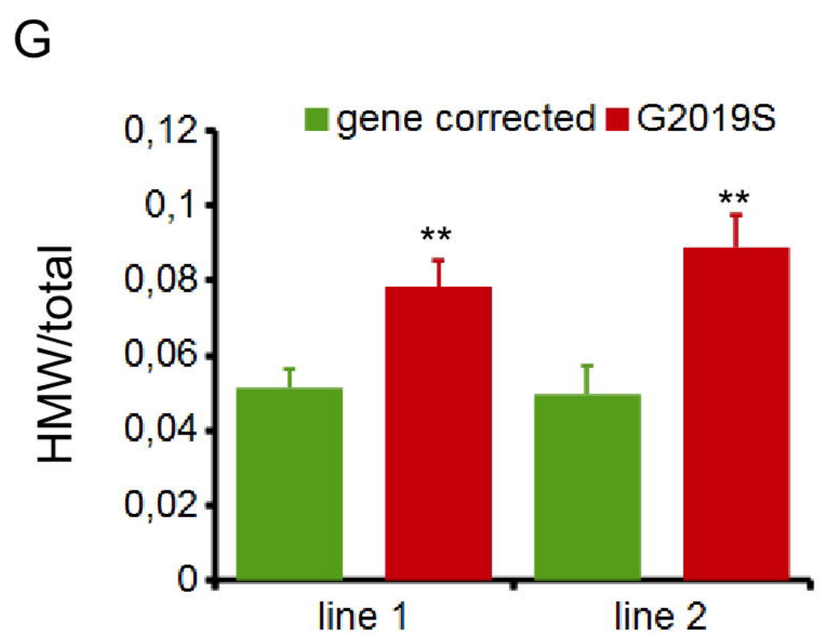
G
gene corrected
G2019S
HMW/total
0,12
0,1
0,08
0,06
0,04
0,02
0
**
**
line 1
line 2

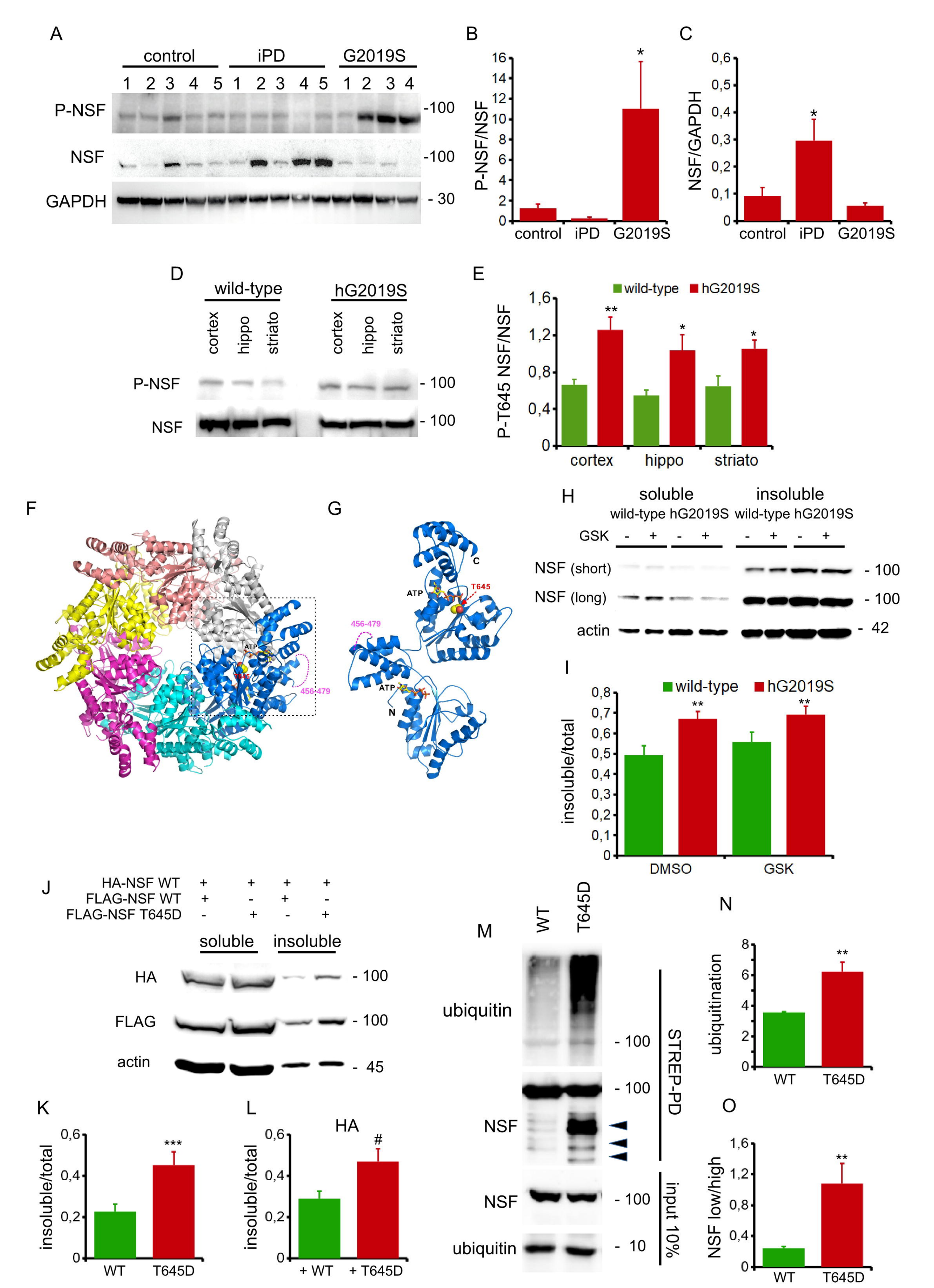
A
control
iPD
G2019S
1 2 3 4 5 1 2 3 4 5 1 2 3 4
P-NSF
NSF
GAPDH
-100
-100
- 30
B
P-NSF/NSF
control
iPD
G2019S
C
NSF/GAPDH
control
iPD
G2019S
D
wild-type
hG2019S
cortex
hippo
striato
P-NSF
NSF
- 100
- 100
E
wild-type
hG2019S
P-T645 NSF/NSF
cortex
hippo
striato
F
ATP
T645
456-479
G
C
ATP
T645
456-479
ATP
N
H
soluble
insoluble
wild-type hG2019S wild-type hG2019S
GSK
NSF (short)
NSF (long)
actin
- 100
- 100
- 42
I
wild-type
hG2019S
insoluble/total
DMSO
GSK
J
HA-NSF WT
FLAG-NSF WT
FLAG-NSF T645D
soluble
insoluble
HA
FLAG
actin
- 100
- 100
- 45
K
insoluble/total
WT
T645D
L
HA
insoluble/total
+ WT
+ T645D
M
WT
T645D
ubiquitin
NSF
NSF
ubiquitin
- 100
- 100
- 100
- 10
STREP-PD
input 10%
N
ubiquitination
WT
T645D
O
NSF low/high
WT
T645D

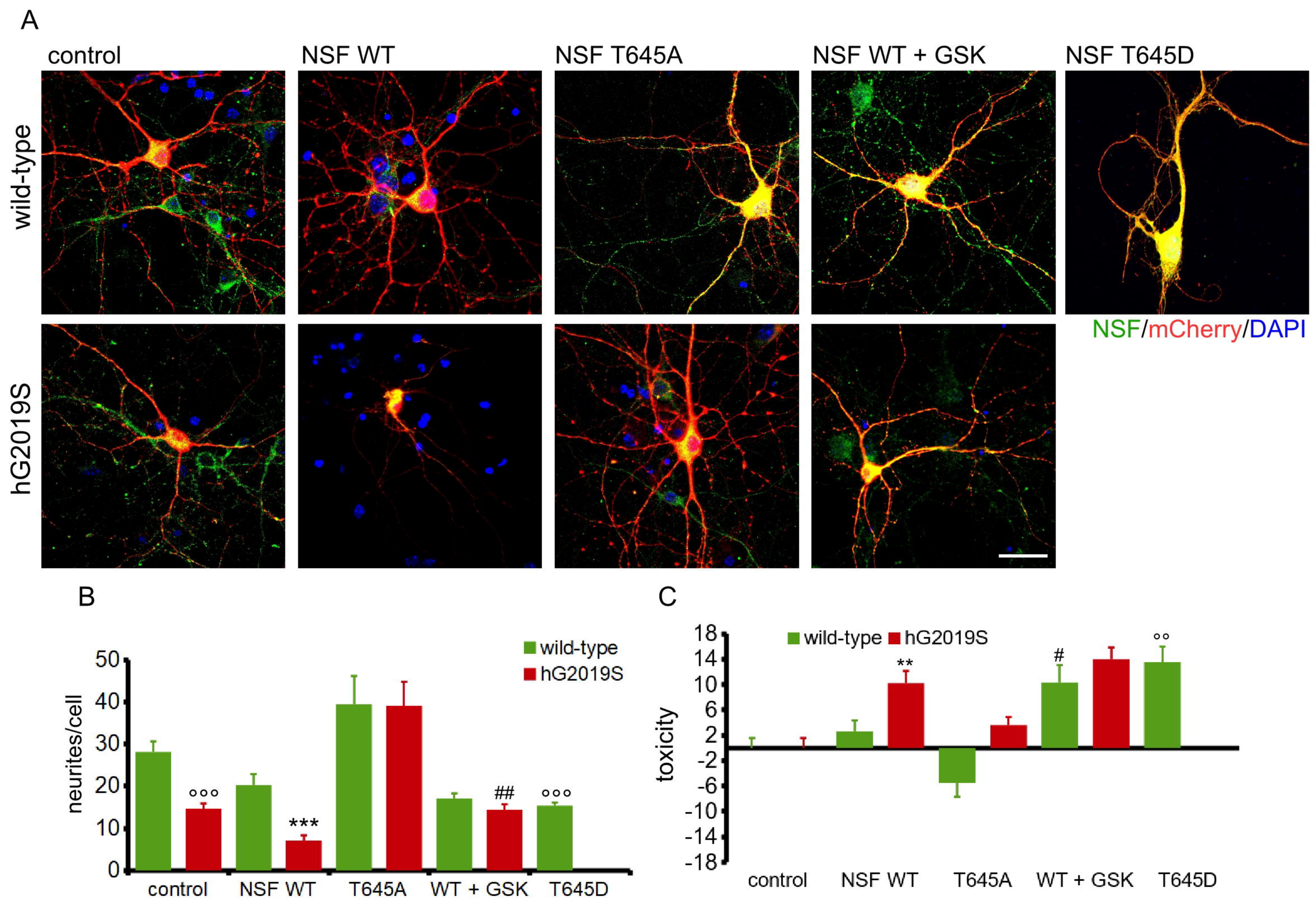
A
control
NSF WT
NSF T645A
NSF WT + GSK
NSF T645D
wild-type
hG2019S
NSF/mCherry/DAPI
B
wild-type
hG2019S
neurites/cell
50
40
30
20
10
0
°°°
***
##
°°°
control
NSF WT
T645A
WT + GSK
T645D
C
wild-type
hG2019S
toxicity
18
14
10
6
2
-2
-6
-10
-14
-18
**
#
°°
control
NSF WT
T645A
WT + GSK
T645D

A

NSF

TH

cleaved caspase 3

water

wild-type

hG2019S

trehalose 1%

wild-type

hG2019S

B

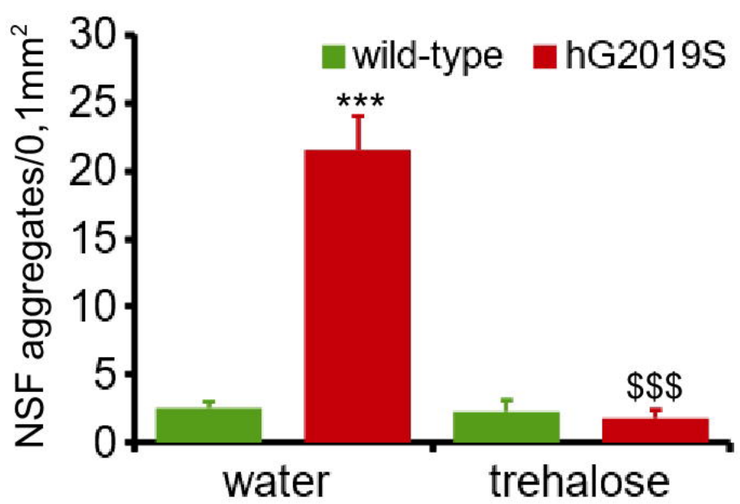

C

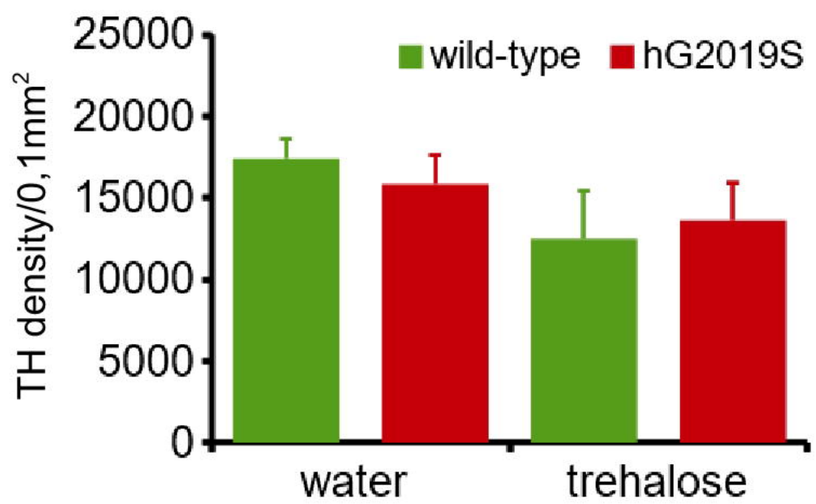

D

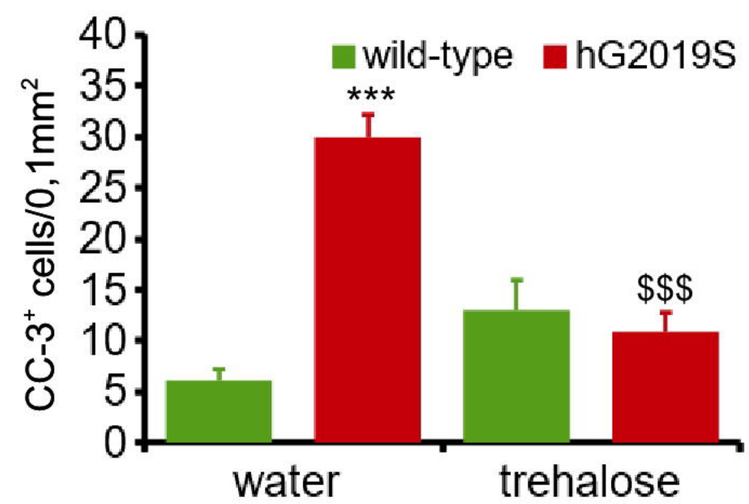

A

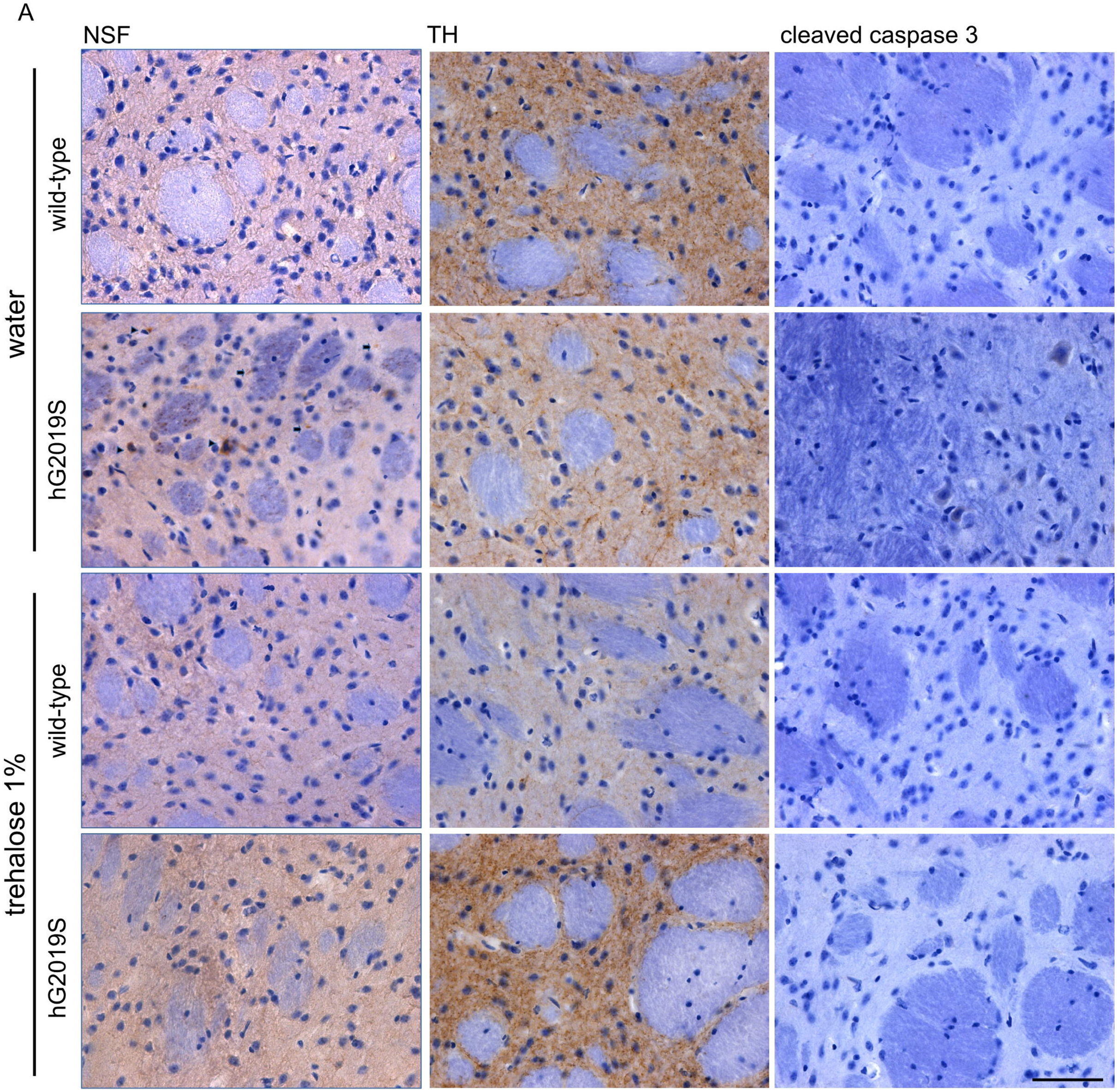
NSF
TH
cleaved caspase 3
water
wild-type
hG2019S
trehalose 1%
wild-type
hG2019S

B

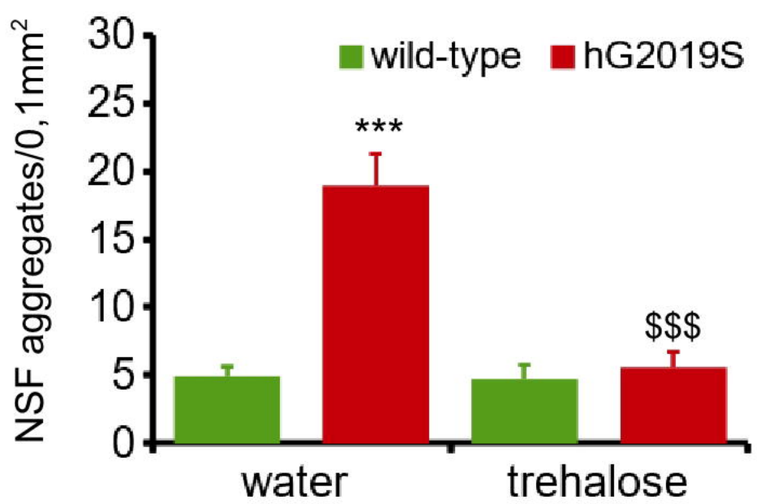
NSF aggregates/0,1mm²
30
25
20
15
10
5
0
wild-type
hG2019S
***
$$$
water
trehalose

C

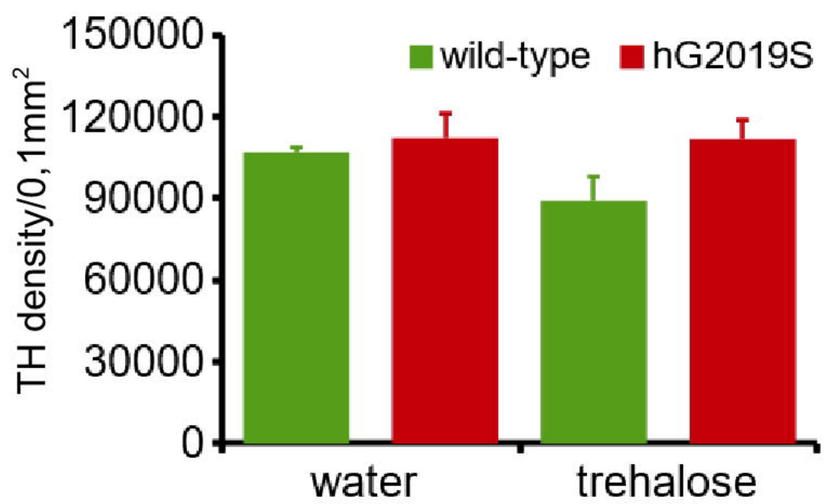
TH density/0,1mm²
150000
120000
90000
60000
30000
0
wild-type
hG2019S
water
trehalose

D

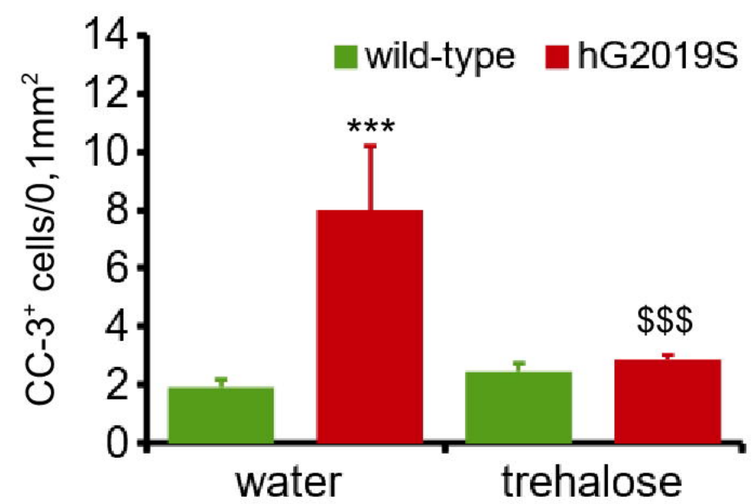
CC-3⁺ cells/0,1mm²
14
12
10
8
6
4
2
0
wild-type
hG2019S
***
$$$
water
trehalose

A

cortex

hippocampus

NSF

cleaved caspase 3

NSF

cleaved caspase 3

water

wild-type

hG2019S

trehalose 1%

wild-type

hG2019S

B

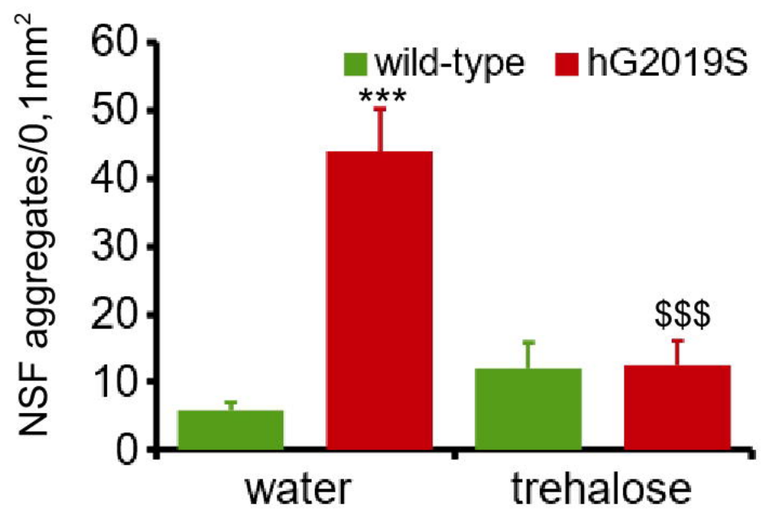

C

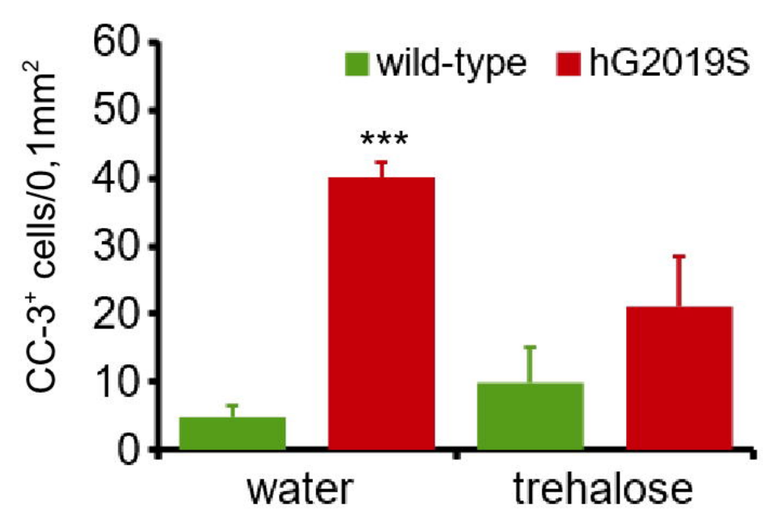

D

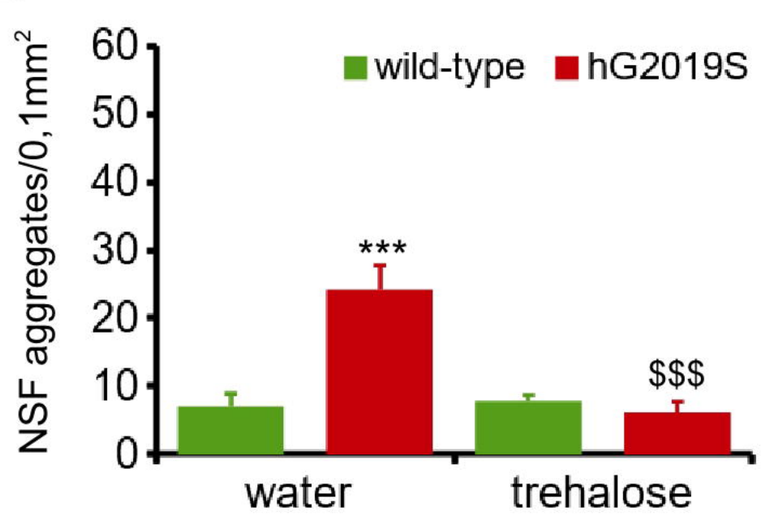

E

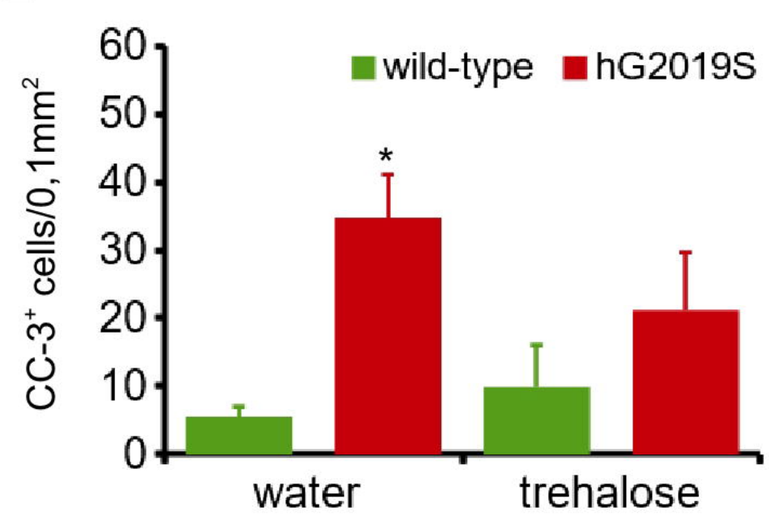

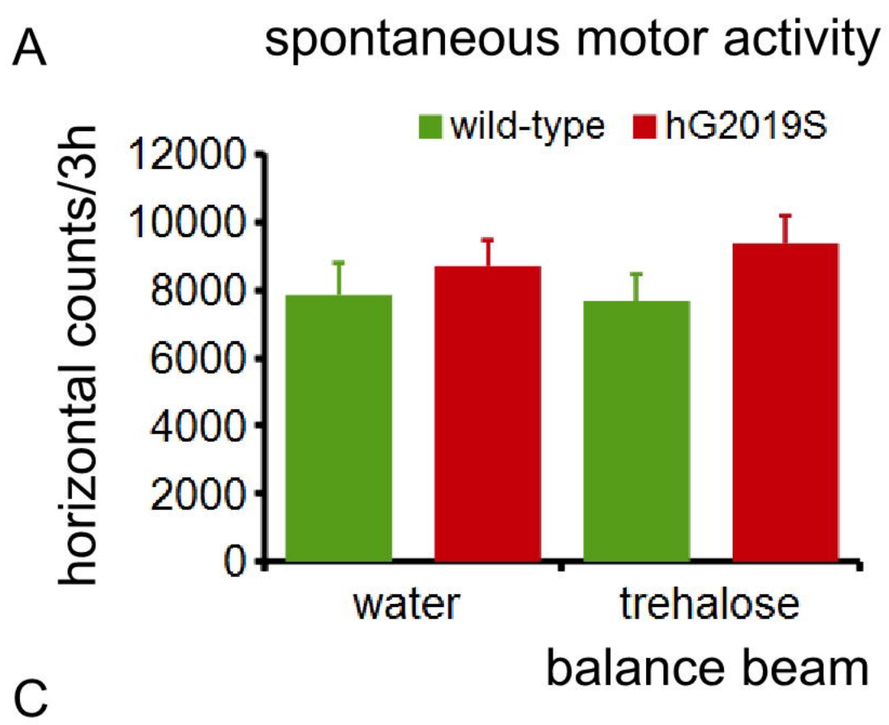
A
spontaneous motor activity
wild-type
hG2019S
horizontal counts/3h
12000
10000
8000
6000
4000
2000
0
water
trehalose
balance beam

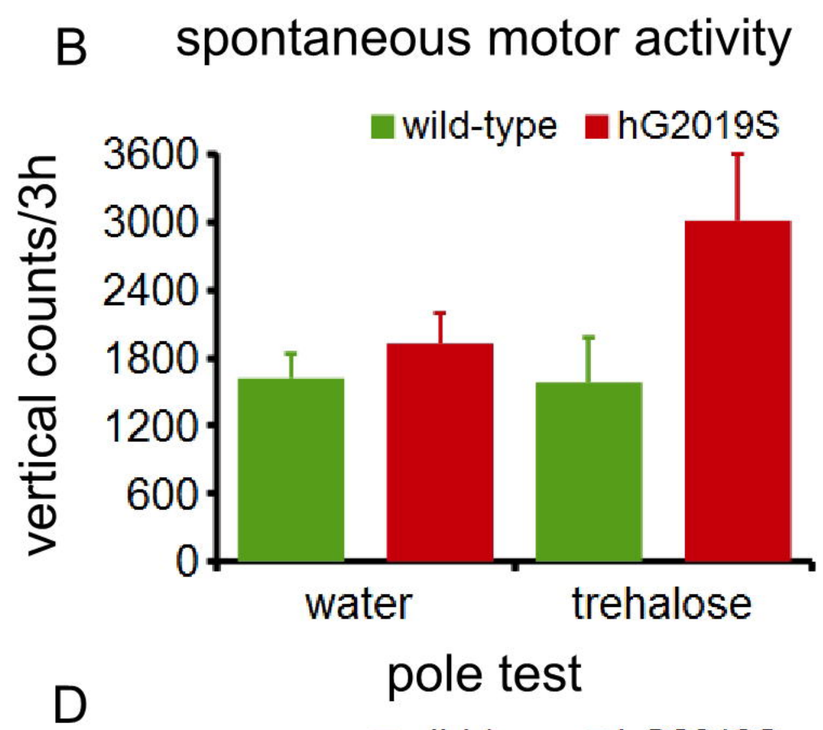
B
spontaneous motor activity
wild-type
hG2019S
vertical counts/3h
3600
3000
2400
1800
1200
600
0
water
trehalose
pole test

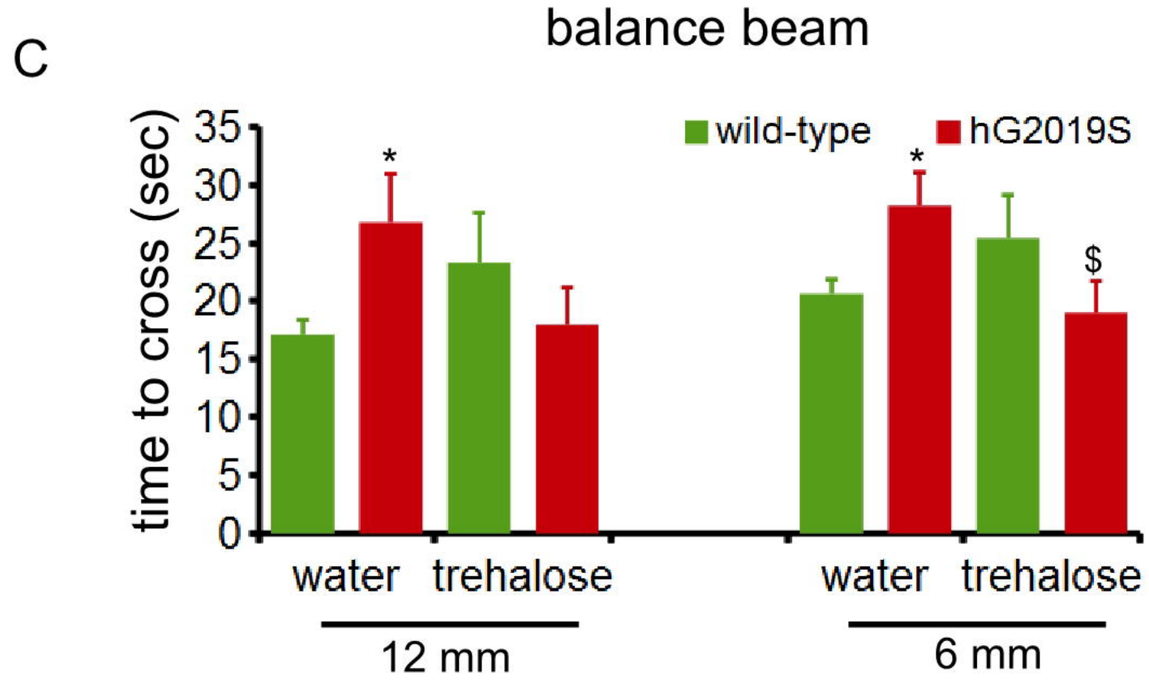
C
wild-type
hG2019S
time to cross (sec)
35
30
25
20
15
10
5
0
*
*
$
water
trehalose
water
trehalose
12 mm
6 mm

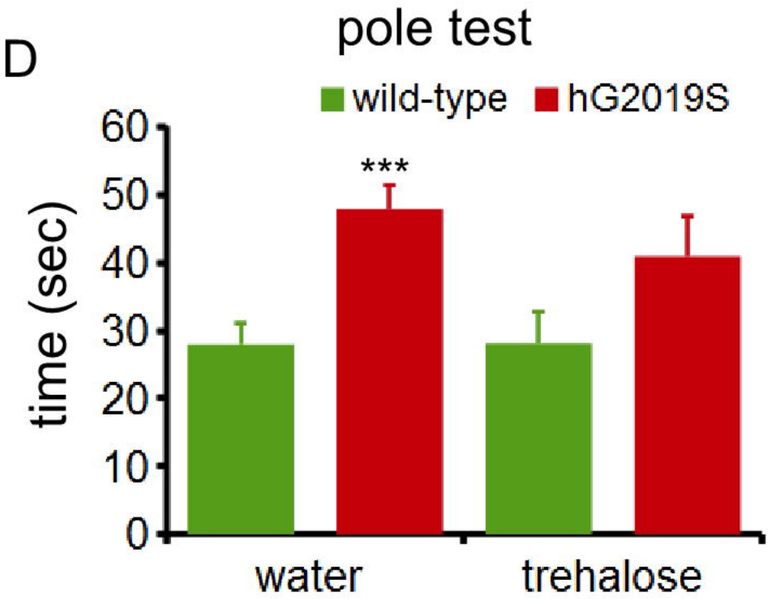
D
wild-type
hG2019S
time (sec)
60
50
40
30
20
10
0
***
water
trehalose

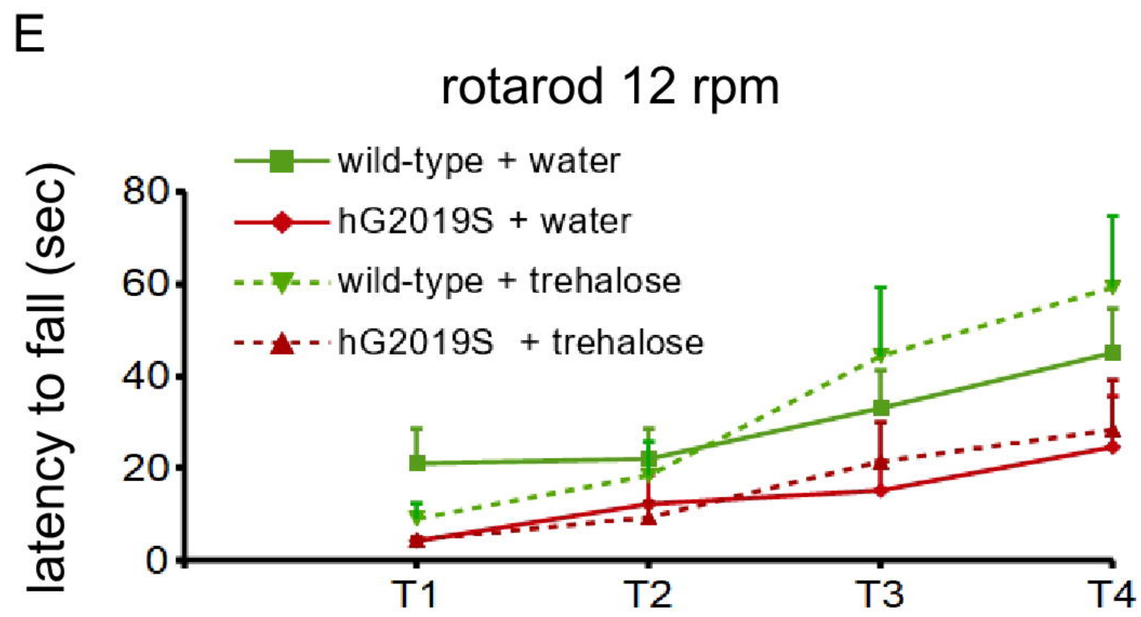
E
rotarod 12 rpm
wild-type + water
hG2019S + water
wild-type + trehalose
hG2019S + trehalose
latency to fall (sec)
80
60
40
20
0
T1
T2
T3
T4

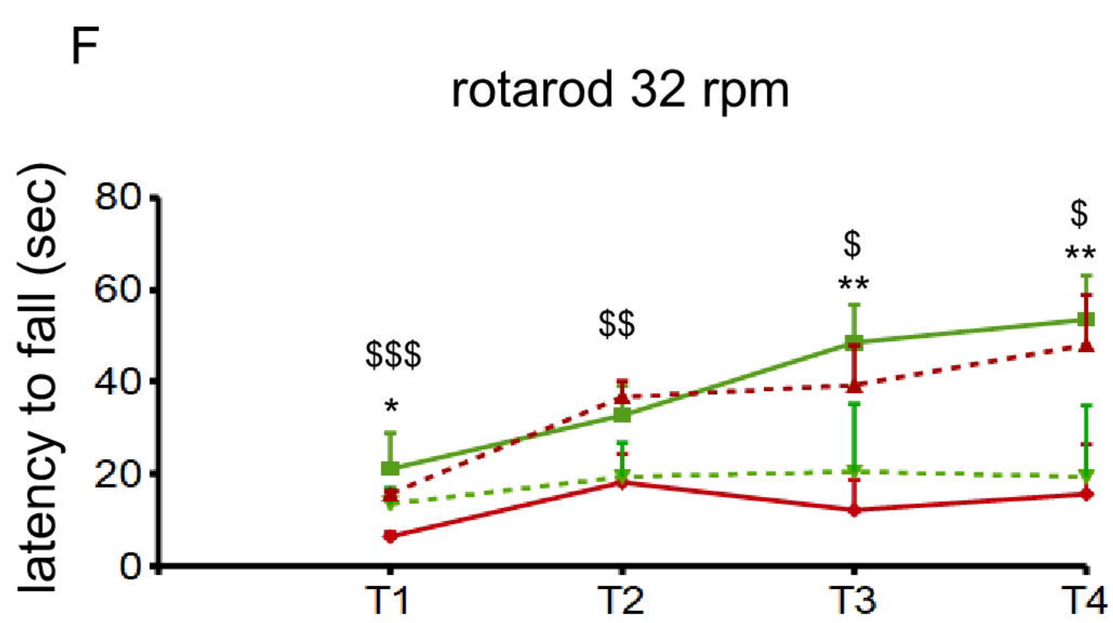
F
rotarod 32 rpm
latency to fall (sec)
80
60
40
20
0
$$$
*
$$
$
**
$
**
T1
T2
T3
T4

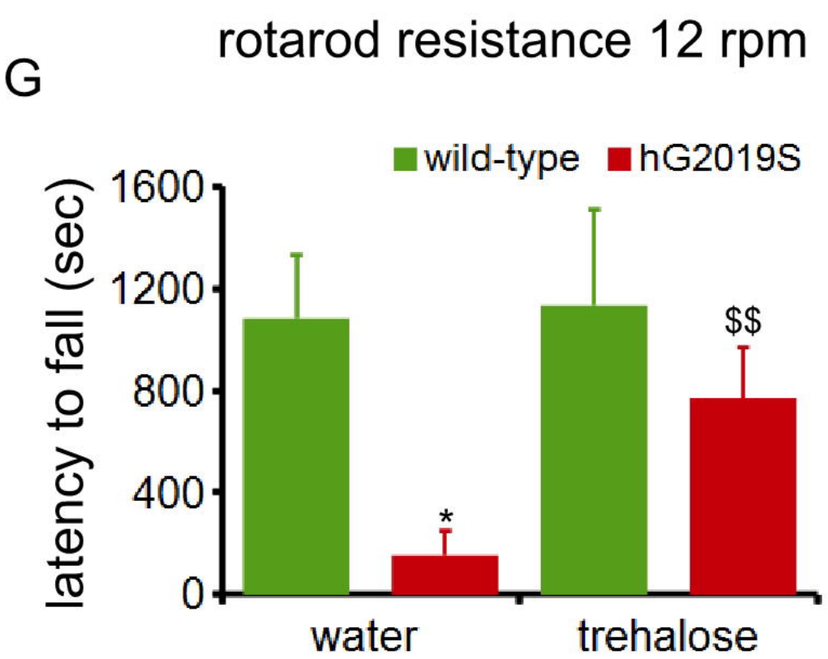
G
rotarod resistance 12 rpm
wild-type
hG2019S
latency to fall (sec)
1600
1200
800
400
0
*
$$
water
trehalose

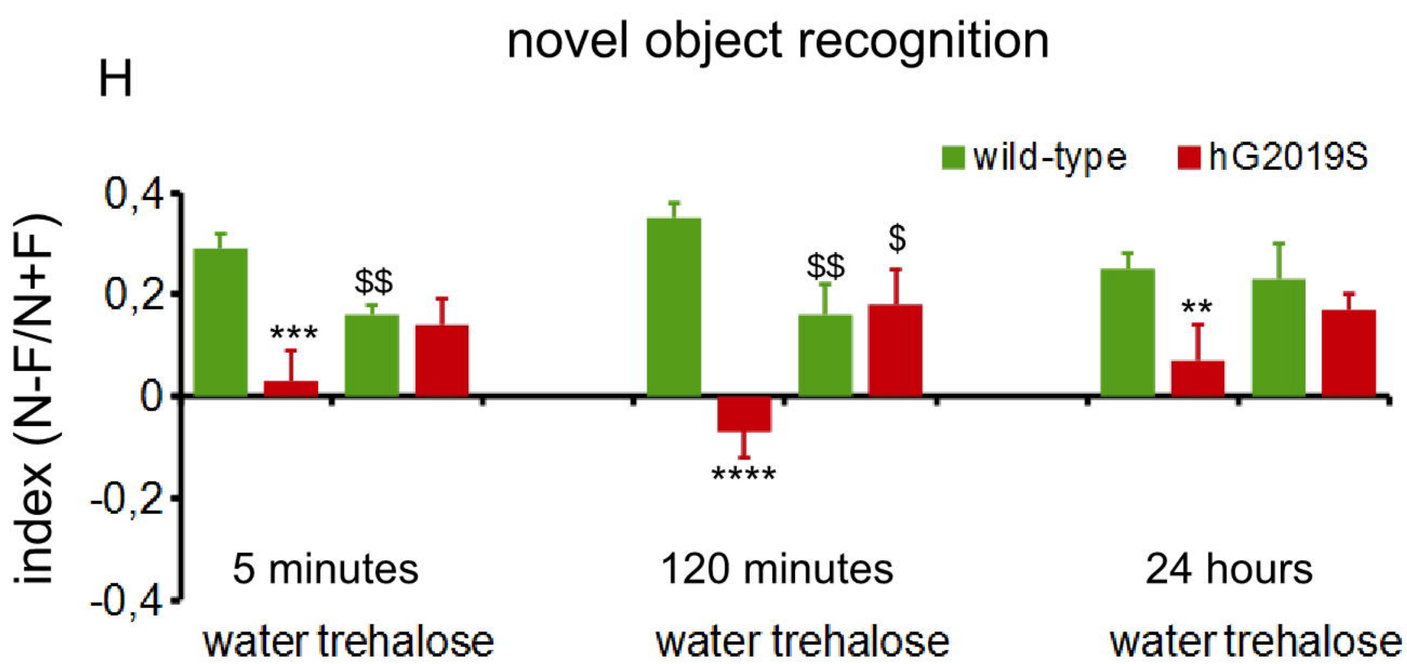
H
novel object recognition
wild-type
hG2019S
index (N-F/N+F)
0,4
0,2
0
-0,2
-0,4
***
$$
****
$$
$
**
5 minutes
120 minutes
24 hours
water trehalose
water trehalose
water trehalose